Applied Energy 347 (2023) 121388

Contents lists available at ScienceDirect

Applied Energy

journal homepage: www.elsevier.com/locate/apenergy

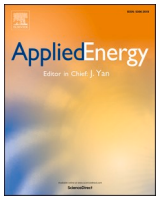

Maximizing onboard power generation of large-scale railway vibration energy harvesters with intricate vehicle-harvester-circuit coupling relationships

Liwei Dong [a,b,*], Guobiao Hu [c], Jie Yu [a,d], Chaoyang Zhao [b], Shuai Qu [b,e], Yaowen Yang [b,*]

[a] Institute of Rail Transit, Tongji University, Shanghai 201804, China
[b] School of Civil and Environmental Engineering, Nanyang Technological University, 50 Nanyang Avenue, Singapore 639798, Singapore
[c] Internet of Things Thrust, The Hong Kong University of Science and Technology (Guangzhou), Nansha, Guangzhou, Guangdong 511400, China
[d] Zhuzhou CRRC Times Electric Co., Ltd., Zhuzhou 412001, China
[e] Train and Track Research Institute, State Key Laboratory of Traction Power, Southwest Jiaotong University, Chengdu 610031, China

HIGHLIGHTS

- A railway energy harvesting system is experimentally validated for energy harvesting, conversion and storage.
- The harvester modeling considers nonlinear mechanical friction for better performance prediction.
- An energy harvesting circuit is implemented with the integration of the MPPT algorithm and power management module.
- A vehicle-harvester-circuit system model is developed by considering the intricate interactions involved.
- An onboard control strategy is proposed to enhance harvester power by up to 60%.

ARTICLE INFO

Keywords:
Railway vibration energy harvesting
Maximizing onboard performance
Energy harvesting circuit
System modeling
Vehicle dynamics

ABSTRACT

Large-scale vibration energy harvesters (VEHs) have the potential to produce power of tens of watts and offer a distributed and flexible power supply for onboard devices in unpowered freight wagons. However, research on railway vibration energy harvesting systems (VEHSs) is often limited to individual points and lacks systematic exploration and optimization. This paper proposes a systematic modeling approach for VEHS that considers the intricate interaction and coupling in the vehicle-harvester-circuit system. Firstly, a model is established for a rotary electromagnetic VEH using the equivalent circuit method, with mechanical friction considered and identified via the Equilibrium Optimizer (EO) to improve prediction accuracy. The energy harvesting circuit (EHC) incorporating a bridge rectifier, a DC/DC converter, and a power management module with a speed-driven maximum power point tracking (MPPT) algorithm is designed for efficient energy extraction and storage under stochastic vehicle suspension vibrations. In addition, the freight wagon is modeled spatially based on railway vehicle-track dynamics, accounting for the nonlinearities of primary and secondary suspensions to obtain more accurate vibration response and mechanical interaction with the harvester-circuit module for the coupling of the whole system. Finally, a performance-enhanced control strategy is proposed with the dynamic tuning of voltage coefficient to maximize onboard harvestable energy based on the developed system model. The results indicate that the harvester power can be increased by up to 60%, and the force decreased by up to 11% at various vehicle speeds and loads. The prototype of the whole railway VEHS with MPPT closed-loop control is implemented in the embedded environment, and its engineering-oriented design will significantly improve the system robustness and practicality in onboard environments.

* Corresponding authors.
E-mail addresses: victor@tongji.edu.cn (L. Dong), cywyang@ntu.edu.sg (Y. Yang).

https://doi.org/10.1016/j.apenergy.2023.121388
Received 19 April 2023; Received in revised form 22 May 2023; Accepted 31 May 2023
Available online 21 June 2023

1. Introduction

Railway is one of the major transportation modes worldwide, promoting regional, national, and international exchanges and development [1]. It is favored for its low-pollution, cost-effectiveness and reliability in transporting goods and people over long distances. In the past decades, high-speed and heavy-load railway freight transportation has become an evident tendency to improve transportation efficiency. However, higher requirements for vehicle monitoring and braking performance are triggered to ensure safe and reliable operations [2]. Standard freight wagons are not equipped with electrical lines, leading to a lack of continuous and economical power supplies for novel braking devices and onboard monitoring. Traditional battery-powered solutions are inconvenient due to the need for regular charging and replacement. Hence, seeking a flexible and sustainable power supply scheme is the key to unlocking more smart devices in freight wagons and promoting their intelligent transformation [3].

Energy harvesting is an emerging technology that converts ambient solar [4], wind [5,6], vibration [7,8], thermal [9] and magnetic field energy [10] into electricity for self-powered applications. This technology has achieved great successes in numerous fields such as ocean engineering [11,12], aerospace engineering [13], biomedical engineering [14], and road engineering [15]. The rapid railway development triggers a growing demand for energy harvesting technology to reduce manual maintenance in inconvenient power supply scenarios or remote railways. Fortunately, railway systems are abundant of various renewable energy sources, providing favorable condition for energy harvesting. Solar and wind energy are typically given priority for railway self-powered applications. Tairab et al. [16] proposed a solar-wind hybrid energy harvester installed along the railway with a rotation mechanism to follow the solar radiation better. Pan et al. [17] developed a wind barrier consisting of coaxial contrarotating wind turbines for train crosswind harvesting. Rahman et al. [18] designed a miniaturized windmill nanogenerator enhancing its practicability in subway tunnels by hybridizing electromagnetic, triboelectric, as well as piezoelectric mechanisms. Yang et al. [19] utilized the temperature difference between the rail and the soil and manufactured an innovative railway fastener using thermoelectric materials to heat rail pads to alleviate their performance degradation in extremely freezing weather. Kuang et al. [20] noticed magnetic field energy generated by the alternating current flow through electrified rails, and harvested it based on the electromagnetic induction principle.

Stochastic vibrations widely exist in railway vehicles, rails, and nearby infrastructures. Energy harvesting from railway vibrations is a promising self-powered approach with the advantages of simple design, low cost, and small size [21,22]. It is an interdisciplinary field encompassing mechanics, electronics, control, and vehicle dynamics. The design of vibration energy harvesters (VEHs) mainly focuses on the development of piezoelectric [23,24], electromagnetic [25,26], triboelectric [27,28] mechanisms, and their hybridizations [29,30]. Railway-specific VEHs usually adopt the first two schemes. Shan et al. [31] conceived a frequency up-conversion method for a stack piezoelectric energy harvester (PEH) to ensure that resonant response can be excited under low-frequency rail excitation. Wang et al. [32] developed a compact axlebox-mounted PEH to harness bogie lateral vibrations. It achieved a low-frequency bandwidth of 1–11 Hz by leveraging a hybrid nonlinear mechanism and effectively powered wireless sensor nodes. Yang et al. [33] optimized the resonant frequencies of single-mass piezoelectric cantilevers to accord with the first two rail vibration dominant frequencies, thus enhancing high-frequency energy harvesting performance. Wang et al. [34] fabricated a multifunctional electromagnetic VEH with the configuration of a rolling magnet to expand bandwidth for rail corrugation sensing. Kim et al. [35] proposed a resonant electromagnetic VEH by the interaction between magnets, and enabled it to power the wireless nodes on high-speed trains with parameter optimization. Gong et al. [36] integrated an interesting electromagnetic VEH with a cylindrical Halbach array into an axlebox bearing, which can generate a 4.3 W output at 1200 r/min speed.

The feasibility in powering wireless sensor nodes using small-scale VEHs has been fully proven. However, railway devices such as railway signal lights, switches, control units of electronically controlled pneumatic (ECP) braking systems, and train-tail devices usually require higher power supplies, far more than milliwatts. As a result, large-scale VEHs are demanded in these applications. Researchers usually exploit mechanical transmission to convert, rectify and amplify the vibration, which is then used to drive a rotary generator at high speeds to produce significant power outputs of up to tens of watts. For rail-side applications, Zhang et al. [37] conceived a large-scale VEH with a mechanical motion rectifier (MMR) driven by a rack-pinion pair to harness bidirectional small track vibrations, achieving a maximum efficiency of 60% in lab tests. Pan et al. [38] developed a smart railroad tie with half-wave VEH for unidirectional vibration energy harvesting, and the novel structure was validated with a maximum mechanical efficiency of about 80%. Lin et al. [39] designed a bevel-gear-based MMR for a large-scale VEH, and conducted field tests with a 6.9 W average power obtained during a train passing by at 64 km/h. Zhang et al. [40] realized the function of mechanical motion rectification with twin pairs of scissor linkage and slider mechanisms. Their designed harvester exhibited a considerable efficiency of 73.38% in lab tests. There are also some large-scale VEHs for onboard devices. Pan et al. [41] developed a large-scale rack-pinion-based VEH to harvest vibration energy from freight car suspension, which realized a field-test performance of 1.3 W at 30 km/h train speed. Li et al. [42] conceived an MMR with twin slider-crank mechanisms and obtained a peak/average efficiency of 56%/43% in bench tests. Fan et al. [43] proposed H-shaped harvesters for harnessing the kinetic energy from the relative displacement of couplers and fast storing it in supercapacitors. The generated power is sufficient to light up 80 LEDs and 10 types of sensors, enabling real-time vehicle safety monitoring.

Various novel mechanical structures offer numerous possibilities for designing large-scale railway VEHs. However, the mechanical friction in VEHs poses limitations on their performance. When assessing the measured mechanical efficiencies of large-scale railway VEHs, it is found that the mechanical friction, which often amounts to one-third to two-thirds of energy loss [40,42,43], cannot be ignored and significantly affects the potential performance of harvesters. Thereby, further theoretical research is required to improve model prediction accuracy and optimize the efficiency of VEHs.

Energy harvesting circuit (EHC) is another crucial technology that promotes VEHs towards practical applications. Piezoelectric harvesters with large internal resistance cannot be efficiently used or stored using conventional electronics. To address this issue, EHCs such as synchronous charge extraction (SCE) [44], parallel synchronized switch harvesting on inductor (P–SSHI) [45], series synchronized switch harvesting on inductor (S–SSHI) [46], and synchronized switch harvesting on capacitors (SSHC) [47] have been developed to boost the power outputs from PEHs. Correspondingly, the research on energy extraction circuits extends to electromagnetic and triboelectric VEHs [48,49]. However, their feasibility is only validated under regular vibrations, and their actual performance under stochastic railway vibration needs further exploration. Consequently, Balato et al. [50] proposed an EHC for a small-scale electromagnetic VEH with the development of maximum power point tracking (MPPT) technology adjusting circuit voltages according to the vehicle vibration characteristics at different running speeds. Costanzo et al. [51] combined the Perturb & Observe and the fractional open-circuit voltage technologies to improve the adaptability of the MPPT algorithm for suspension harvesters. Moreover, they proposed another scheme based on an active AC/DC converter where the duty cycle is related to the generator speed, and it will be a promising solution when combined with low-power management techniques [52]. Jung et al. [53] developed an EHC with a multifunctional single-stage power converter to deal with the issues of

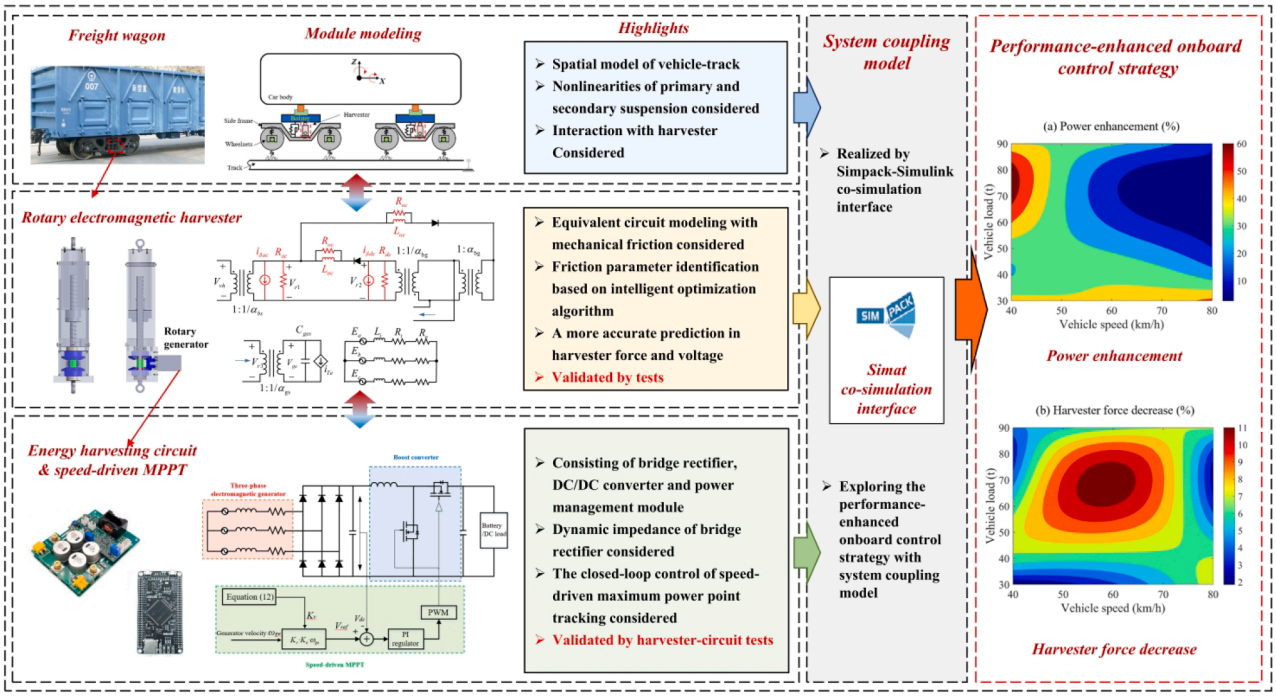

Fig. 1. Vehicle-harvester-circuit system modeling and performance-enhanced onboard control strategy.

impedance matching and power management, which achieved a conversion efficiency of 86 % with a 2 mm amplitude and 2 Hz frequency excitation. However, these designs ignored the interaction between harvesters and railway vehicles.

From the perspective of vehicle dynamics with harvesters, Yuan et al. [54] simplified the PEH installed between the ballast and sleeper as a spring in the dynamic model. Gao et al. [55] considered the mass and inertia moment effects of the rail-borne electromagnetic VEH in the rail system, and found that the dominant frequency of track vibration shifts about 54 Hz. Pan et al. [56] established the mass-spring-damper model of large-scale rack-pinion-based VEH and coupled it with the track system. The results showed no obvious dynamic impact on the track with the harvester equipped, mainly because the harvester's damping is far less than that of railway tracks.

Large-scale onboard VEHs are capable of producing significant and continuous power output compared to other harvesting technologies. However, due to their damping characteristics, which can be of the same order as the vehicle shock absorber, the railway vibration energy harvesting system (VEHS) becomes a mutually coupled system comprising the vehicle, harvester, and circuit. Most of the existing research separately focused on specific aspects of this system, while a systematic exploration and optimization are lacking, leading to gaps and challenges towards practical engineering applications. These include: (1) inadequate attention to the mechanical friction in large-scale VEHs, which restricts performance improvement, and is often ignored in modeling work due to its strong nonlinearity, resulting in the inaccurate prediction of the harvester efficiency and force; (2) a lack of systematic modeling of vehicle-harvester-circuit to reveal internal coupling and energy transfer laws; and (3) insufficient study of the control strategy of large-scale VEHs to integrate closely with actual onboard environments.

In this paper, we present a comprehensive approach to modeling a large-scale VEHS by considering practical factors and intricate vehicle-harvester-circuit coupling. We then explore the harvester control strategy for maximizing the harvestable energy in onboard environments. Additionally, the prototype of the whole railway VEHS with large-scale VEH and EHC under MPPT closed-loop control is manufactured according to structural constraints and power supply demand of freight wagons for the validation of our work. It is worth mentioning that the EHC developed based on a synchronous 4-Switch DC/DC control chip integrates functions of MPPT, voltage conversion, and battery charge management, which could be a mature and generic scheme for energy extraction from large-scale VEHs. The research process is illustrated in Fig. 1. The novel contributions of this study are: (1) implementation and experimental validation of a full-scale railway VEHS to realize a complete process of energy harvesting, conversion and storage; (2) development of a large-scale VEH model with nonlinear mechanical friction considered using equivalent circuit method, along with a parameter identification approach based on the Equilibrium Optimizer (EO), to enhance the prediction accuracy of harvester force and voltage; (3) integration of an EHC with the speed-driven MPPT algorithm and power management module to efficiently utilize and manage irregular energy flow from large-scale VEHs under stochastic vehicle vibrations; (4) creation of a systematic vehicle-harvest-circuit model that considers the nonlinearities in primary and secondary suspensions of freight wagon and mechanical interaction with the harvester-circuit module; and (5) proposal of an onboard control strategy with the dynamic tuning of voltage coefficient based on the system model to improve harvester power output by up to 60% while reducing harvester force by up to 11%.

The contents of the rest of this paper are organized as follows. **Section 2** introduces the harvester circuit model with mechanical friction considered and identified. **Section 3** describes the EHC and the speed-driven MPPT algorithm. **Section 4** presents the prototypes of large-scale VEH and EHC, and conducts experiments for system validation. **Section 5** establishes the vehicle-harvester-circuit model and explores the onboard control strategy. Finally, concluding remarks are summarized in **Section 6**.

2. Harvester and its modeling

The large-scale harvester in the vehicle-harvester-circuit system is a crucial component, and it interacts mechanically with the vehicle suspension and electrically with the energy harvesting circuit. The accuracy of the harvester model will directly affect the solution of vehicle suspension vibration and electrical signals in the energy harvesting circuit under coupling relationships. Mechanical friction usually accounts for one-third to two-thirds of energy loss in large-scale harvesters

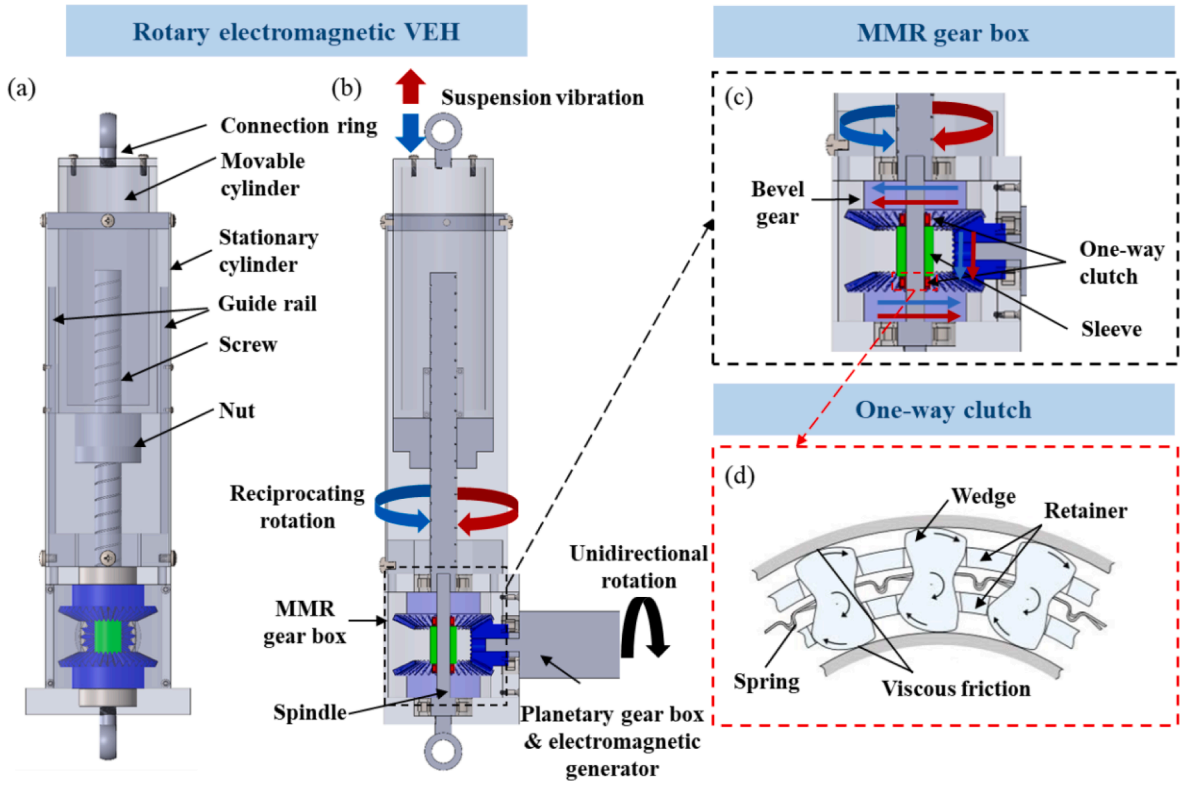

Fig. 2. Rotary electromagnetic VEH based on nut-screw and mechanical motion rectifier.

[40,42,43], which has become one of the most important factors restricting efficiency improvement, but it is rarely discussed in the harvester modeling due to its strong nonlinearity. Considering mechanical friction in modeling is essential to improve the prediction accuracy of mechanical and electrical behaviors. In this section, with the introduction of harvester, the works mainly focus on two aspects: (1) development of the equivalent circuit model of a large-scale railway energy harvester with the consideration of nonlinear mechanical friction including the Coulomb friction (CF) and viscous damping (VD) in all mechanical transmissions and the electromagnetic generator; (2) proposal of an identification approach for nonlinear friction parameters with the combination of the equivalent circuit model, test results and intelligent optimization algorithm.

2.1. Rotary electromagnetic vibration energy harvester

In the railway VEHS, a rotary electromagnetic VEH is the main device for harnessing the vibration energy of wagon suspension, as depicted in Fig. 2. The VEH is mounted between the bolster and side frame of railway freight wagons through connecting rings at both ends. It converts a portion of the secondary suspension vertical vibrations of freight wagons, which would be dissipated as heat by wedges, into electricity to power onboard devices. The harvester is a typical electromechanical coupling system, mainly composed of a ball screw, a mechanical motion rectifier (MMR) gearbox, a planetary gearbox, and a permanent magnet synchronous generator. The ball screw, as a reliable vibration-to-rotation mechanism, converts the upward and downward suspension vibration into bidirectional rotation. The MMR gearbox has been proven to enhance the efficiency of stochastic vibration harvesting [39,57], and consists of upper and lower bevel gears integrating two one-way clutches with opposite installations, and a right bevel gear that transmits the motion to the generator. It is the core component to rectify the bidirectional rotation of the lead screw into unidirectional rotation. The planetary gearbox amplifies the output unidirectional rotation velocity of the MMR gearbox to ensure the high-speed and high-efficiency working state of the generator. Fig. 2**(b) and (c)** illustrate the detailed working principle of the rotary electromagnetic VEH. When the secondary suspension vibrates downward, the vibration is imposed on the top connecting ring, driving the movable cylinder downward. The guide rail fixed inside the stationary cylinder ensures that vertical motion does not deviate. Meanwhile, the nut below the movable cylinder drives the screw to rotate counterclockwise (top view), and the spindle maintains the same rotation with the screw by a key connection. The lower bevel gear engages with the one-way clutch and plays the power one to drive the right bevel gear and the electromagnetic generator to rotate clockwise (left view). The upper bevel gear separates from the one-way clutch and is driven by the right bevel gear. Conversely, assuming that the movable cylinder moves upward, the screw rotates clockwise (top view), and the upper one-way clutch engages with the bevel gear, so that the lower and right bevel gears become follower gears, but their rotation direction is unchanged. Therefore, regardless of the vibration direction, the clockwise rotation of generator is unchanged (left view), avoiding frequent commutation and realizing the bidirectional vibration energy harvesting, thereby improving the system efficiency.

2.2. Equivalent circuit modeling considering mechanical friction

For a simpler construction of complex nonlinear relationships in the harvester and better conjunction with circuit and control modules, the equivalent circuit modeling method [58] is exploited to develop the harvester model and reveal the internal mechanical friction. The three main modules, including the nut-screw pair, MMR gearbox, and planetary gearbox and their corresponding equivalents in the electrical domain, are shown in Fig. 3. There are some basic principles between the mechanical–electrical analogies: force/torque corresponds to current signals; velocity/rotation velocity is equivalent to voltage signals; damping values correspond to reciprocals of resistance values; stiffness values are equal to reciprocals of inductance values; and mass/inertia corresponds to capacitors.

The nut-screw mechanism realizes the vibration-to-rotation function

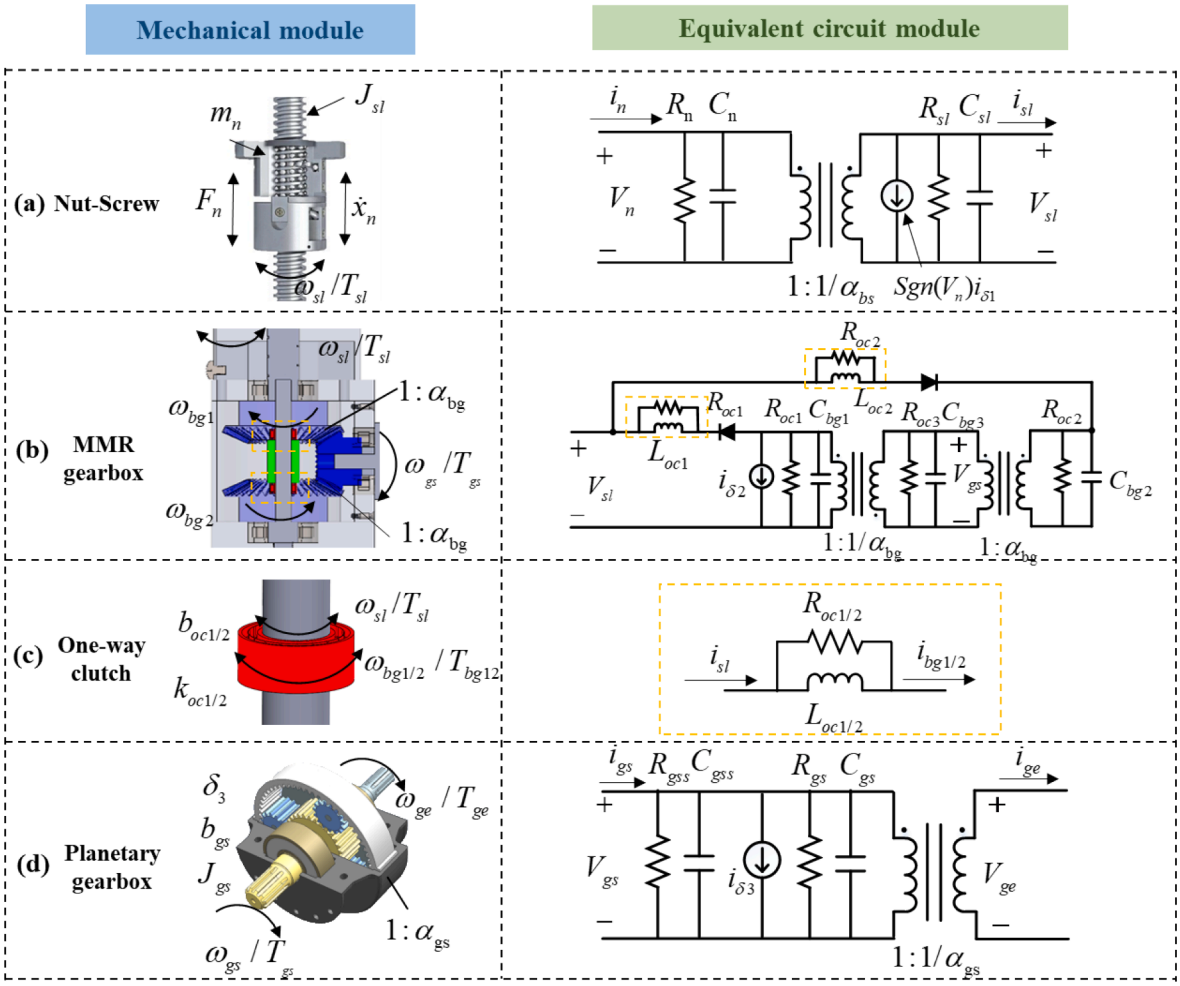

Fig. 3. Equivalent circuit modeling of mechanical modules in the harvester.

with a transmission ratio of α_{bs}, which equals a voltage transformer in the electrical domain. Herein, the CF in the rotary side is considered as a constant torque δ_1 and related to screw lead velocity, corresponding to a current source with the value of $Sgn(V_{sl})\ i_{\delta 1}$. The VD of nut and lead screw b_n and b_{sl} are considered and presented as the resistances of R_n and R_{sl} in the electrical domain.

The MMR in the mechanical domain plays a similar role to the rectifier in the electrical domain; thereby, it is modeled as two diodes to convert alternating-current (AC) signals to direct-current (DC) signals. One-way clutches are the main power transmission elements in MMR, which inevitably results in friction loss. They are expressed as resistance-inductance parallel models with the consideration of equivalent torsional damping and stiffness. In addition, the equivalent CF and VD are also given consideration in the MMR module.

Similarly, the planetary gearbox module is modeled as a voltage transformer with a transmission ratio of α_{gs}, where the mechanical friction of gear transmission is considered in the form of CF and VD. The correspondences of harvester parameters in mechanical and electrical domains are listed in Table 1.

The mechanical equation of a three-phase permanent magnet synchronous generator can be expressed as

$$\begin{cases} T_{ge} = T_e + b_{ge}\omega_{ge} + J_{ge}\dot{\omega}_{ge} \\ i_{ge} = i_e + V_{ge}/R_{ge} + C_{ge}\dot{V}_{ge} \end{cases} \tag{1}$$

where T_e and i_e are the electrical torque of the generator; b_{ge} and $1/R_{ge}$ represent the mechanical friction coefficient of the generator; and J_{ge} and C_{ge} are the generator inertia in the mechanical and electrical domains, respectively.

The electrical torque of the generator can be represented as

$$T_e = K_t\left[i_a\sin\theta + i_b\sin\left(\theta - \frac{2}{3}\pi\right) + i_c\sin\left(\theta + \frac{2}{3}\pi\right)\right] \tag{2}$$

The relationship of the generator electromotive force with the rotation velocity and external load can be expressed as

$$\begin{cases} E_a = K_e\omega_{ge}\sin\theta = L_i\dfrac{di_a}{dt} + (R_i + R_e)i_a \\ E_b = K_e\omega_{ge}\sin\left(\theta - \dfrac{2}{3}\pi\right) = L_i\dfrac{di_b}{dt} + (R_i + R_e)i_b \\ E_c = K_e\omega_{ge}\sin\left(\theta + \dfrac{2}{3}\pi\right) = L_i\dfrac{di_c}{dt} + (R_i + R_e)i_c \end{cases} \tag{3}$$

where E_a, E_b, E_c are the electromotive force of the generator; K_t and K_e correspond to the torque and voltage constants, respectively; $\theta = \int p\omega_{ge}$ is the electrical angle with p being the number of polar pairs; L_i represents the internal inductance of the generator; R_i and R_e are the internal and external resistances, respectively; and i_a, i_b, i_c represent phase current.

A complete equivalent circuit model of rotary electromagnetic VEH is illustrated in Fig. 4, where in addition to the above three main modules, the mechanical friction loss of the guide rail is also considered with CF and VD. In such a model, the most important issue is that too many unknown friction parameters are difficult to measure and determine. Hence, with the order reduction and simplification, the model can be

Table 1
Analogies between the elements in the mechanical and electrical domains.

Module	Mechanical domain	Electrical domain	Description
Nut-screw	F_n, T_{sl}	i_n, i_{sl}	Force/torque of nut and lead screw
	$\dot{x}_n$, ω_{sl}	V_n, V_{sl}	Velocity/rotation velocity of nut and lead screw
	δ_1	$i_{\delta 1}$	Coulomb friction of lead screw
	b_n, b_{sl}	$1/R_n$, $1/R_{sl}$	Viscous damping of nut and lead screw
	m_n, J_{sl}	C_n, C_{sl}	Mass/rotational inertia of nut and lead screw
	α_{bs}	α_{bs}	Transmission ratio of nut-screw mechanism
MMR gearbox (one-way clutches integrated)	T_{bg1}, T_{bg2}, T_{bg3}, T_{bgs}	i_{bg1}, i_{bg2}, i_{bg3}, i_{bgs}	Torque of upper bevel gear, lower bevel gear, right bevel gear and input shaft of planetary gearbox
	ω_{bg1}, ω_{bg2}, ω_{bg3}, ω_{bgs}	V_{bg1}, V_{bg2}, V_{bg3}, V_{bgs}	Rotation velocity of upper bevel gear, lower bevel gear, right bevel gear and input shaft of planetary gearbox
	δ_2	$i_{\delta 2}$	Coulomb friction of mechanical motion rectifier gearbox
	b_{bg1}, b_{bg2}, b_{bg3}	$1/R_{bg1}$, $1/R_{bg2}$, $1/R_{bg3}$	Viscous damping of upper bevel gear, lower bevel gear and right bevel gear
	J_{bg1}, J_{bg2}, J_{bg3}	C_{bg1}, C_{bg2}, C_{bg3}	Rotational inertia of upper bevel gear, lower bevel gear and right bevel gear
	α_{bg1}, α_{bg2}	α_{bg1}, α_{bg2}	Transmission ratio between bevel gear 1 and bevel gear 3, and between bevel gear 2 and bevel gear 3
	b_{oc1}, b_{oc2}	$1/R_{oc1}$, $1/R_{oc2}$	Equivalent torsional damping of upper one-way clutch and lower one-way clutch
	k_{oc1}, k_{oc2}	$1/L_{oc1}$, $1/L_{oc2}$	Equivalent torsional stiffness of upper one-way clutch and lower one-way clutch
Planetary gearbox	ω_{ge}	V_{ge}	Rotation velocity of generator shaft
	T_{ge}	i_{ge}	Torque of generator shaft
	δ_3	$i_{\delta 3}$	Coulomb friction of planetary gearbox
	b_{gs}	$1/R_{gs}$	Viscous damping of planetary gearbox
	J_{gs}	C_{gs}	Equivalent rotational inertia of planetary gearbox
	α_{gs}	α_{gs}	Transmission ratio of planetary gearbox

shown in Fig. 5. Because of the planetary gearbox with a large transmission ratio, the generator rotates at a high velocity, and the contribution of the generator inertia J_{ge} to the harvester inertial force is far greater than other parts, thereby the capacitors in the circuit, except for C_{gs}, are omitted. The mechanical motions before the MMR gearbox are bidirectional, which are viewed as the AC part of the circuit, while the unidirectional motions in the MMR gearbox and its backend are regarded as the DC part. The VD and CF are represented by one equivalent parameter in the AC and DC parts, respectively.

The equivalent VD and CF in the AC part are defined as R_{ac} and $i_{\delta ac}$ in the simplified circuit model, which can be expressed as

$$1/R_{ac} = 1/R_{gr} + 1/R_n + 1/\alpha_{bs}^2 R_{sl} \tag{4}$$

$$i_{\delta ac} = i_{\delta 0}/\alpha_{bs} + i_{\delta 1} \tag{5}$$

Correspondingly, the equivalent VD and CF in the DC part are defined as R_{dc} and $i_{\delta dc}$, which can be represented as

$$1/R_{dc} = (1/R_{bg1} + 1/R_{bg2}) + (1/R_{bg3} + 1/R_{gss} + 1/R_{gs})/\alpha_{bg}^2 + 1/\alpha_{bg}^2\alpha_{gs}^2 R_{ge} \tag{6}$$

$$i_{\delta dc} = i_{\delta 2} + \alpha_{bg} i_{\delta 3} \tag{7}$$

Hence, in the simplified circuit model, the physical quantities relative to the mechanical friction should be determined, including the equivalent VD R_{ac} and CF $i_{\delta ac}$ in the AC part, the equivalent VD R_{dc} and CF $i_{\delta dc}$ in the DC part, and the equivalent torsional damping R_{oc} and stiffness L_{oc} of two one-way clutches.

2.3. Mechanical friction parameter identification

In this section, the identification method with an intelligent optimization algorithm is proposed for the mechanical friction parameters in the harvester model. The optimization algorithm exploits Equilibrium Optimizer (EO), which is a novel *meta*-heuristic optimizer based on the volume-mass balance model. It was developed by Faramarzi et al. [59] in recent years, with the advantages of strong search ability and fast convergence. The identification process is illustrated in Fig. 6.

Firstly, the optimization vector is constructed as $\overrightarrow{C}_i = (i_{\delta ac}, i_{\delta dc}, R_{ac}, R_{dc}, R_{oc}, L_{oc})$ with all unknown mechanical friction parameters included, followed by the setting of algorithm parameters and the random generation for particles and populations in EO. Then, the randomly generated friction parameters are injected into the equivalent circuit model. On the other hand, the experimental data, including vibration excitation, harvester force, and harvester voltage are acquired and recorded through the energy harvesting test bench (a detailed introduction of the test bench will be presented in **Section 4.2**). Under the same vibration excitation, the simulation results are calculated based on the model and compared to the test data. The relative errors are evaluated according to:

$$F(\overrightarrow{C}_i) = e = \frac{1}{N}\left[\beta_1 \left|\frac{rms(F_{sim} - F_{\exp})}{rms(F_{\exp})}\right| + \beta_2 \left|\frac{rms(V_{sim}) - rms(V_{\exp})}{rms(V_{\exp})}\right|\right] \tag{8}$$

where N is the number of cases involved in the identification, F_{sim} and F_{exp} represent the simulation and experimental harvester force under the same vibration excitation; V_{sim} and V_{exp} represent the simulation and experimental harvester voltage; β_1 and β_2 are the proportional factors, determining the importance of force and voltage accuracy to the overall evaluation.

This expression comprehensively evaluates the model accuracy based on errors in force and voltage and plays as the fitness function of EO. The accuracy evaluation through multiple cases can reduce the inaccurate evaluation caused by accidental test errors. The force accuracy evaluation based on the RMS errors between simulation and experimental data considers the hysteresis of force caused by mechanical friction. The voltage accuracy evaluation based on the error of the RMS value between simulation and experimental data is because the output phase voltage of the AC generator contains many high-frequency components.

The next step is to update mechanical friction parameters based on EO. The detailed logic of EO can be referred to [59]. By repetitive iteration, the error between simulation and experimental data is reduced. When the relative errors are small enough, the parameters are considered to fit the actual situation. Finally, the optimal mechanical friction parameters and fitness are recorded.

2.4. Identification results

The bound of constructed vectors $\overrightarrow{C}_{\max}$ and $\overrightarrow{C}_{\min}$ are set to (20, 20, 300, 300, 300, 0.1) and (0, 0, 0, 0, 0, 0), respectively. The particle size is 30, and the maximum iteration number is 200. The mechanical friction parameters and fitness during iterations are illustrated in Fig. 7. After

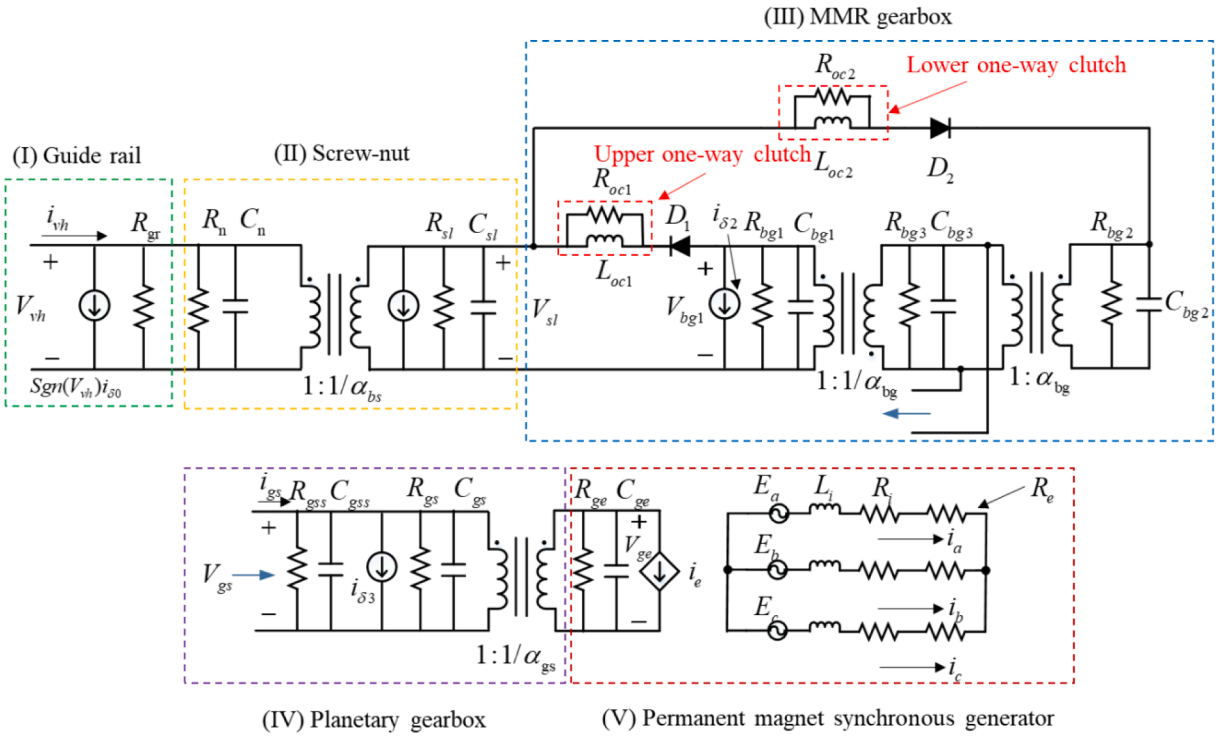

Fig. 4. Equivalent circuit model of the rotary electromagnetic VEH.

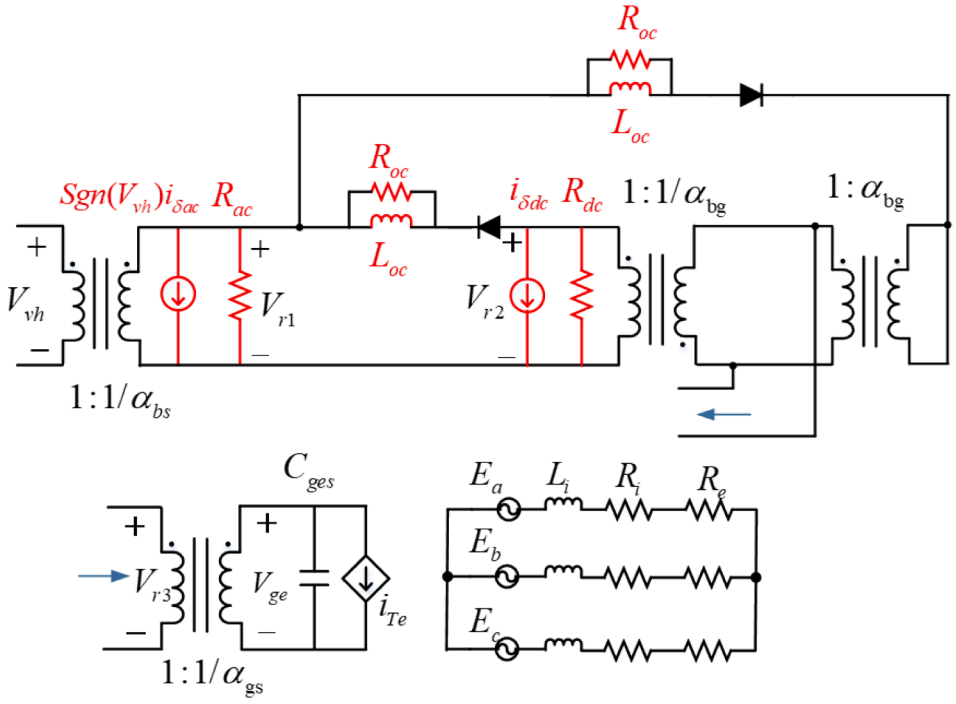

Fig. 5. Simplified circuit model of the rotary electromagnetic VEH.

200 iterations, the final value of the fitness function is 0.06, and the corresponding optimal parameter vector is (0.95, 8.92e-4, 4.64, 47.17, 178.65, 0.053).

The simulation results of the parameter-identified circuit model are compared to the experimental data in other conditions as shown in Fig. 8. Fig. 8**(a) and (c)** illustrate the harvester force and phase voltage under the regular triangular vibration with 0.65 Hz frequency and 6 mm amplitude at 8 Ω external resistance. Fig. 8**(b) and (d)** present those under the regular triangular vibration with 0.95 Hz/4 mm excitation at 16 Ω external resistance. The simulated and experimental forces show a good consistency and no obvious hysteresis, which indicates the proposed model can well compensate for the hysteresis caused by the mechanical friction. However, the displacement sensor is easily impacted when the vibration direction changes, resulting in a certain experimental measurement error. This error component in measured displacement always causes the simulation forces to be slightly larger

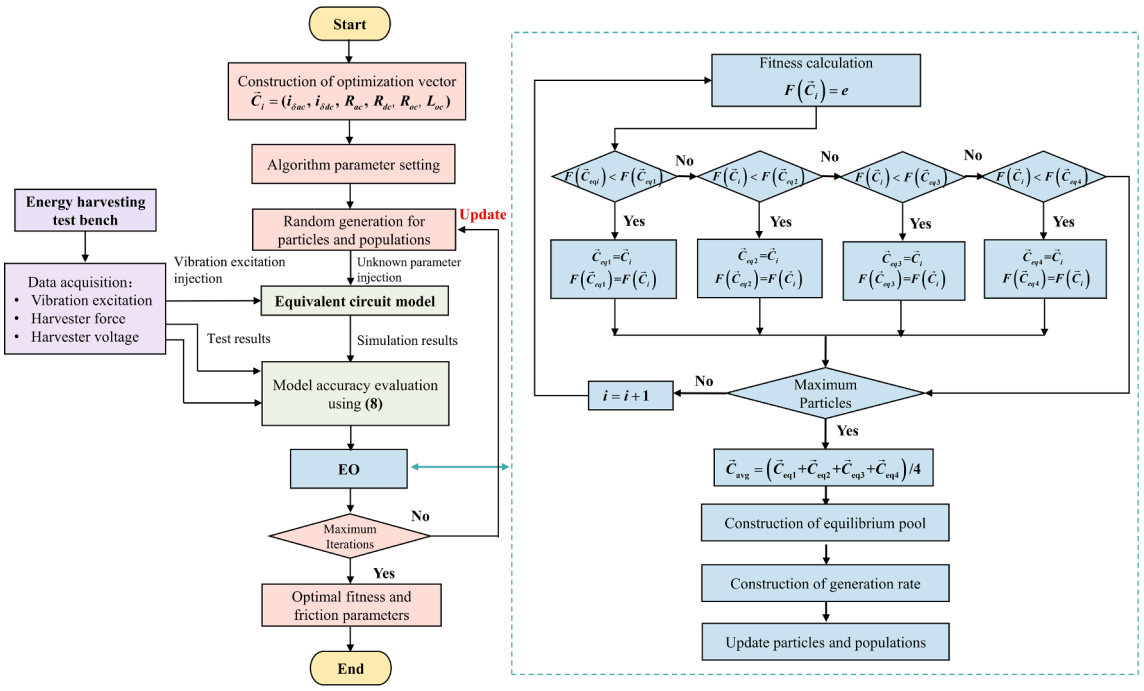

Fig. 6. Mechanical friction parameter identification based on EO.

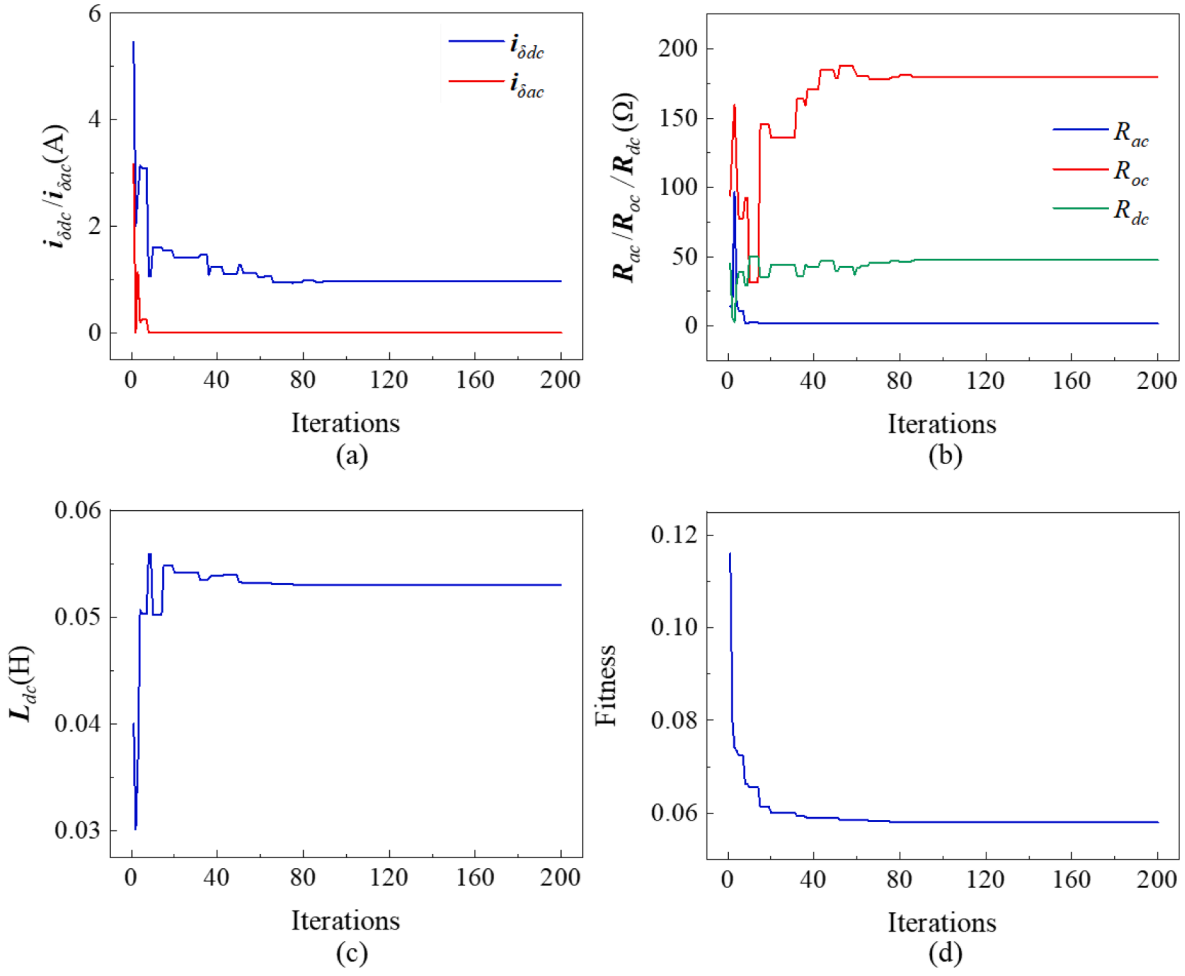

Fig. 7. Parameter identification results: (a) equivalent Coulomb friction values in the AC and DC parts; (b) equivalent viscous damping values in the AC and DC parts, and the equivalent torsional damping value of the one-way clutch; (c) equivalent torsional stiffness value of the one-way clutch; (b) value of the fitness function.

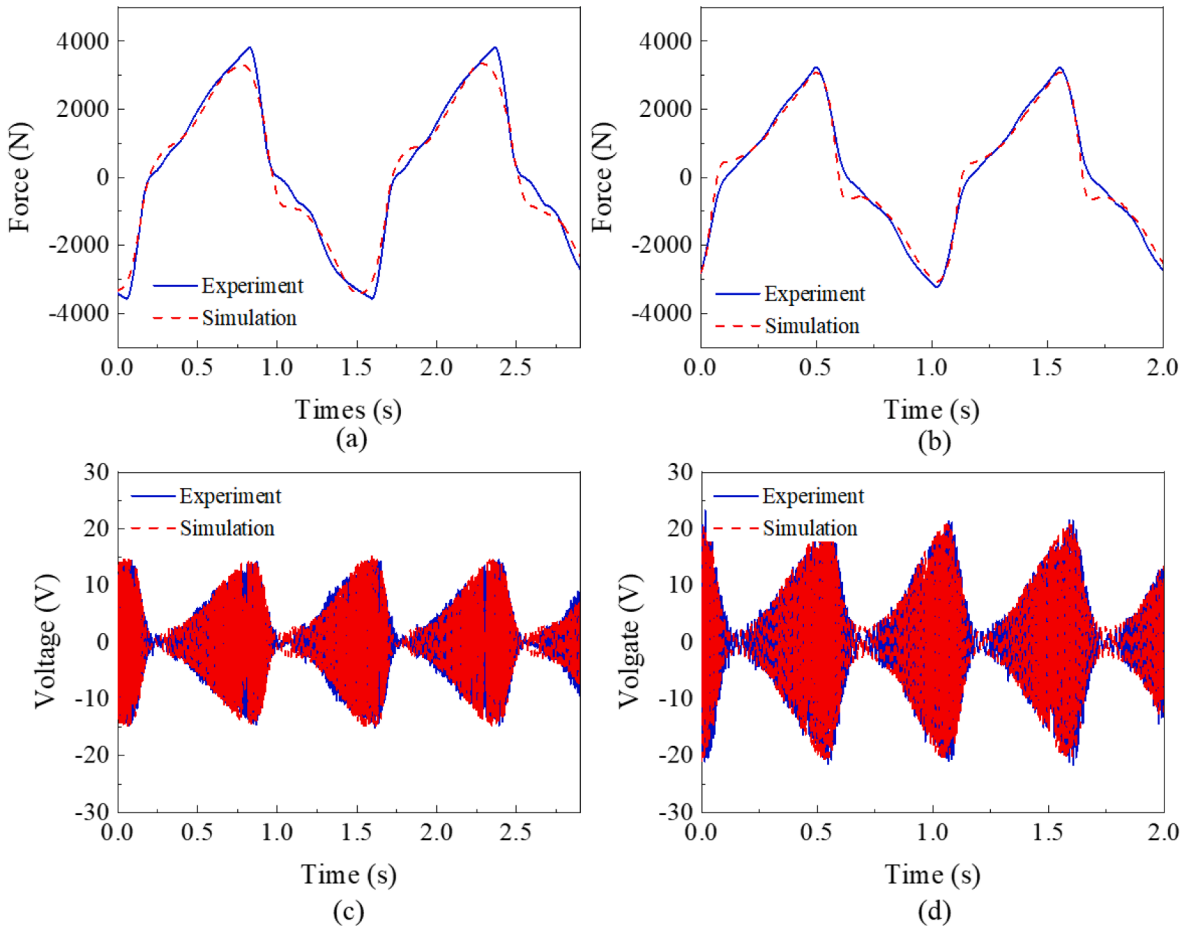

Fig. 8. Comparison between the simulation results predicted by the parameter-identified circuit model and the experimental results: (a) the harvester force in the case of 0.65 Hz/6 mm/8 Ω and (b) 0.95 Hz/4 mm/16 Ω; (c) the harvester phase voltage in the case of 0.65 Hz/6 mm/8 Ω and (d) 0.95 Hz/4 mm/16 Ω.

Table 2
Errors between simulation results based on the parameter-identified circuit model and experimental results.

	Case 1	Case 2
Vibration excitation/ external load	0.65 Hz/6 mm/8 Ω	0.95 Hz/4 mm/16 Ω
Error in force	10.19%	10.87%
Error in voltage	2.55%	0.23%
Comprehensive error evaluation	6.47%	5.55%

than the experimental values when the force direction changes. In addition, the simulated and experimental voltages exhibit high conformity in both the trend and peak values, which can validate the circuit model accuracy. The specific errors of the two cases are listed in Table 2.

3. Energy harvesting circuit

3.1. Circuit design

Large-scale VEHs generate an irregular three-phase AC voltage under stochastic suspension vibrations. Thereby, an EHC, as shown in Fig. 9, is designed to deal with it for efficient energy extraction and storage. The bridge rectifier, with the advantages of low loss and simple structure, is exploited to convert the irregular three-phase AC voltage into irregular DC voltage. With the generator internal impedance affecting actual output voltage, a boost converter is configured with the interface for the MPPT algorithm implemented to solve the impedance matching issue. Then, the subsequent buck/boost converter regulates the irregular DC voltage into a stable one for charging batteries or supercapacitors, thus realizing the harvested energy storage.

3.2. Speed-driven MPPT algorithm

In VEHSs, the MPPT algorithm is commonly used to regulate circuit load and ensure systems have optimal power outputs. Because VEHSs are applied to a stochastic and time-varying vibration environment, the general MPPT algorithms are difficult for quick and accurate tracking. To achieve timely tracking under vehicle suspension vibrations, the concept of the speed-driven MPPT algorithm was proposed in [51,52]. Based on the basic theory in them, herein the optimal voltage of the system is analyzed in an ideal condition.

Assuming the existence of MPPT optimal voltage, the EHC is simplified, as shown in Fig. 10. In a constant vibration velocity input, the rotation velocity and electrical angle can be expressed as

$$\omega_{ge} = \frac{2\pi}{l}\alpha\dot{x} \tag{9}$$

$$\theta = p\omega_{ge}t \tag{10}$$

where l represents the screw lead, and α is the total amplified ratio with mechanical transmission.

Only two diodes are on at any time in the circuit, taking phase a and phase b as an example for analysis. The line voltage between two phases can be expressed as

$$E_{ab}(\theta) = E_a - E_b = \sqrt{3}k_e\omega_{ge}\sin\left(\theta - \frac{\pi}{6}\right) \tag{11}$$

Ignoring the voltage drop through diodes and the internal inductance

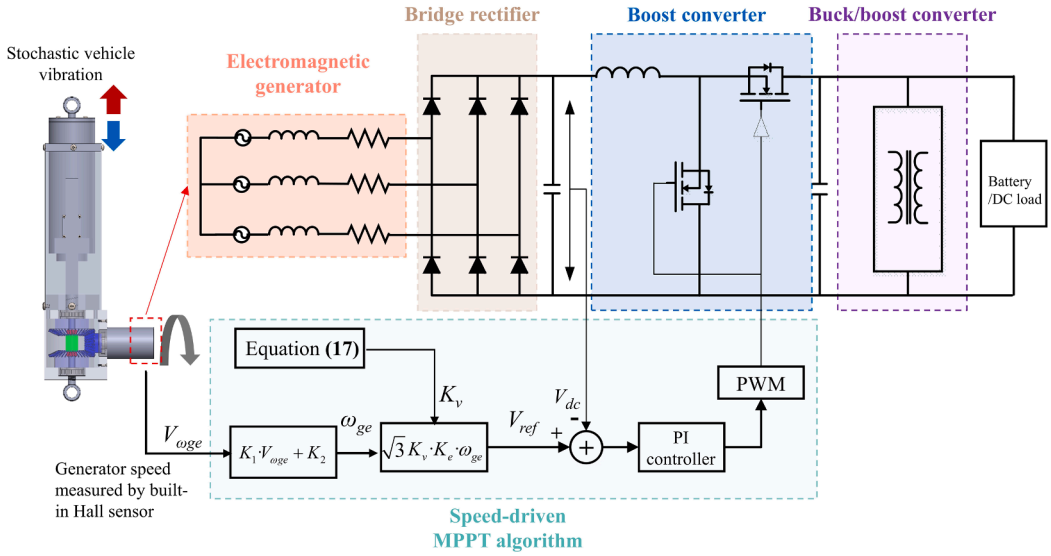

Fig. 9. Configuration of energy harvesting circuit with the speed-driven MPPT algorithm.

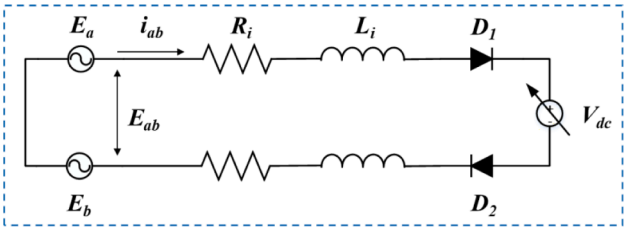

Fig. 10. Simplified energy harvesting circuit.

of the rotary generator, the following relationship exists

$$\frac{V_{dc}}{E_{ab}} = \frac{R_{dc}}{R_{dc} + 2R_{ge}} \tag{12}$$

The obtained DC power related to θ can be expressed as

$$P_{dc}(\theta) = \frac{V_{dc}^2}{R_{dc}} = \frac{V_{dc}(E_{ab}(\theta) - V_{dc})}{2R_{ge}} \tag{13}$$

When the electrical angle is between $[2\pi/3, \pi]$, phases a and b conduct current. The average power generated can be derived as

$$P_{dc} = \frac{3\sqrt{3}k_e\omega_{ge}V_{dc}}{2\pi R_{ge}} - \frac{V_{dc}^2}{2R_{ge}} \tag{14}$$

Differentiating the power expression with respect to V_{dc}

$$\frac{\partial P_{dc}}{\partial V_{dc}} = \frac{3\sqrt{3}k_e\omega_{ge}}{2\pi R_{ge}} - \frac{V_{dc}}{R_{ge}} \tag{15}$$

The optimal voltage V_{dc_MPP} can be obtained and expressed as

$$V_{dc\_MPP} = \frac{3\sqrt{3}}{2\pi}k_e\omega_{ge} = \frac{3\sqrt{3}}{l}n_a k_e \dot{x} \tag{16}$$

Equation (16) indicates that the optimal voltage V_{dc_MPP} is related to $\dot{x}$ or ω_{ge}. Through the layout of the velocity sensor, the speed-driven MPPT algorithm can be realized to maximize extracted energy from the harvester. Because the rotary generator in the proposed harvester is integrated with a Hall sensor, the speed-driven MPPT algorithm is designed with the measurement of the generator rotation velocity.

The speed-driven MPPT algorithm is based on a voltage closed-loop control, as shown in Fig. 9. Firstly, the measurement of the generator rotation velocity is executed by the built-in Hall sensor, and the sensor voltage signal is converted to the actual velocity value. The reference voltage is calculated according to

$$\begin{cases} V_{ref} = \sqrt{3} K_v K_e \omega_{ge} \\ K_v = \dfrac{3}{2\pi} = 0.4775 \end{cases} \tag{17}$$

where K_v is the voltage coefficient, and its optimal analytical value is 0.4775.

Then, the error between V_{ref} and the measured voltage V_{dc} is input to the PI controller for generating the duty cycle signal. The duty cycle signal is transformed to the control signal for switches with the pulse width modulation (PWM), thus enabling the measured voltage V_{dc} is approaching MPPT voltage, and the system finally produces the optimal power output.

The speed-driven MPPT algorithm can achieve an effective maximum power point tracking under stochastic and time-varying vibrations, because the rotary velocity of generator can timely reflect the changes in vibration excitation and the generator working state. The algorithm only needs to calculate the optimal reference voltage for the next moment based on the rotary velocity. Different from the reference [51] using Perturb & Observe to enhance the algorithm adaptability for potential long-time changes of parameters, this paper proposes a novel optimization guideline for the MPPT algorithm with the consideration of the force interaction between the harvester and vehicle suspension. Large-scale VEHs usually have large equivalent damping, which generates a shock absorption effect on the secondary suspension. Thereby, the interaction between the harvester and vehicle suspension is non-negligible. The regulation of voltage coefficient K_v changes the equivalent impedance of circuit, as well as the mechanical property of harvester, thus leading to an impact on coupling effects between the harvester and vehicle suspension. With the validation of energy harvesting system model, the exploration of optimal K_v with intricate vehicle-harvester-circuit coupling relationships will be presented in Section 5.

4. Experimental validation

4.1. Modeling of energy harvesting system

The VEHS model, as shown in Fig. 11, consists of the harvester module, circuit module, and control unit. The harvester model based on

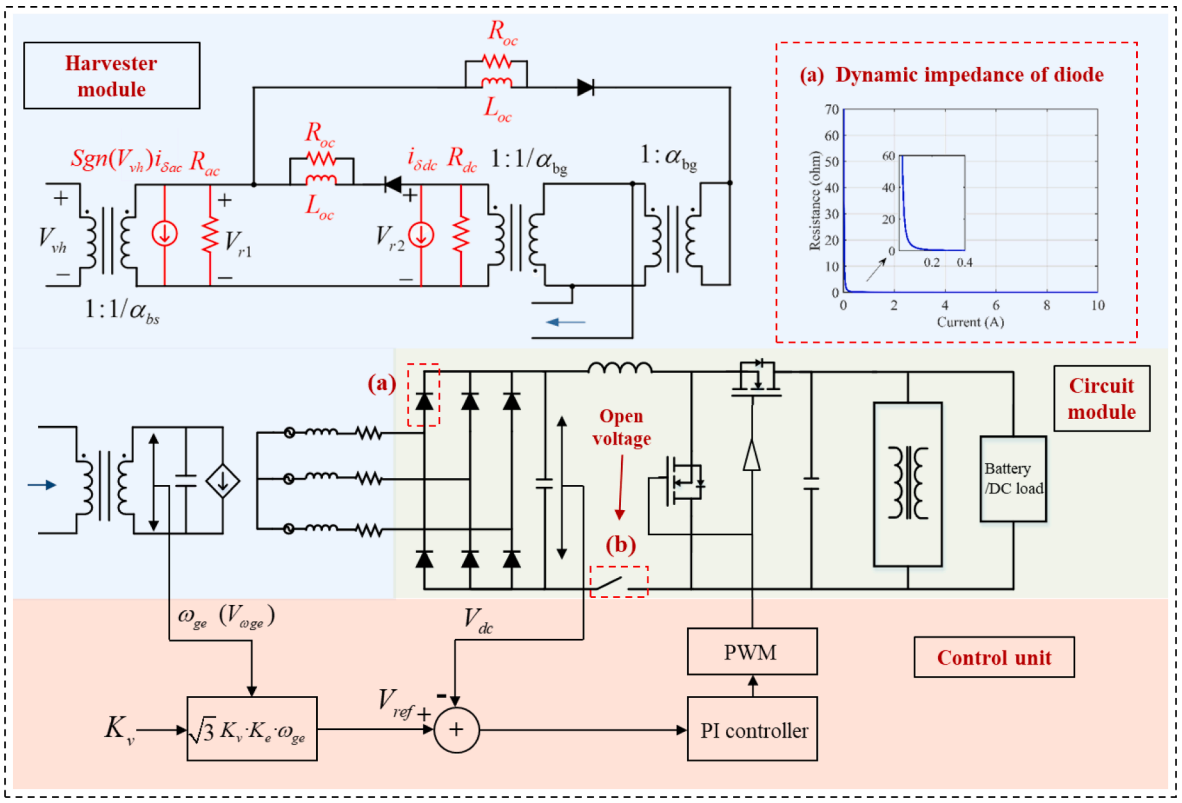

Fig. 11. Model of the energy harvesting system.

the equivalent circuit method can directly integrate with the circuit module and control unit without any additional interface. In this model, the internal induction of the generator, the dynamic impedance of diodes in the bridge rectifier, and the open voltage of DC/DC converter are considered. The dynamic impedance of diodes, as shown in Fig. 11**(a)**, is obtained by their forward voltage-current curves and expressed as

$$R_{di} = a(I_{dc})^{-b} + c \tag{18}$$

where I_{dc} is the forward current of diodes; a, b and c are the parameters for fitting the dynamic impedance curve.

The diode at a low current flow exhibits a large impedance, and considering the dynamic impedance can better simulate the system performance under small vibration excitations. The open voltage of DC/DC converter with a similar effect should also be taken into consideration. The VEHS model with those actual factors and effects considered will have a higher prediction accuracy in mechanical and electrical properties.

4.2. Hardware implementation and experimental setup

The full-scale VEH prototype and EHC are manufactured to validate the VEHS and reveal the interaction between the harvester and circuit. The experimental tests are performed on a horizontal test bench, as shown in Fig. 12. The full-scale harvester prototype is carefully designed and manufactured with full consideration of the constraints and demands of railway onboard applications: (1) The prototype presents an L-shaped structure to save vertical space. Its maximum height of 370 mm strictly adheres to the distance from the upper plane of the bolster to the secondary spring seat in the K6 bogie under the unloaded condition, and its length and width are 165 and 76 mm, respectively. (2) The screw-nut mechanism enables a maximum adjustable height of 83 mm, which can adapt to the relative height variation of the secondary suspension under the wagon unloaded and loaded conditions. (3) The screw-nut mechanism has a smaller backlash, and can easily achieve a large transmission ratio for efficient harvesting of small displacement suspension vibrations. The guide rails reduce the deviation of nut motion in the vertical direction.

The hardware of the EHC with the speed-driven MPPT algorithm is realized for effective energy conversion and storage in actual engineering applications. It includes a bridge rectifier, a microprocessor, an on-chip power management module with DC/DC converter, and a battery pack. The bridge rectifier consists of six diodes of SS56 type with a maximum voltage of 60 V and a maximum forward voltage of 0.7 V at 5 A current flow. The speed-driven MPPT algorithm is developed in the embedded environment and operated in the microprocessor that accounts for the calculation of reference voltage, closed-loop control, generation of PWM, and acquisition of sensing signals. The power management module with DC/DC converter is developed based on the LT8705 chip, which is a synchronous 4-Switch buck-boost DC/DC controller with the functions of voltage conversion, battery charge and basic short circuit protection. It also reserves the interface for the speed-driven MPPT algorithm. With the PWM signal generated by the microprocessor, the MPPT function and power management module can be integrated into a compact circuit. Finally, the stable DC voltage charges the battery pack with a capacity of 13,600 mAh and a standard voltage of 22.2 V. The detailed parameters of VEHS in validation are listed in Table A1.

The horizonal test bench generates arbitrary rotation with a step motor driven under the control of a signal generator. Then, the rotation is transformed to the two-way linear motion of the slider with the ball screw, and the linear motion acts on the harvester by an L-shape fixture. The displacement sensor and force sensor are exploited to measure the vibration and the harvester force. The Hall sensor integrated into the rotary generator accounts for measuring the generator rotation velocity. All the sensor signals and the voltage signals in the EHC are acquired and processed by the microprocessor and displayed on the PC via wireless signal transmission.

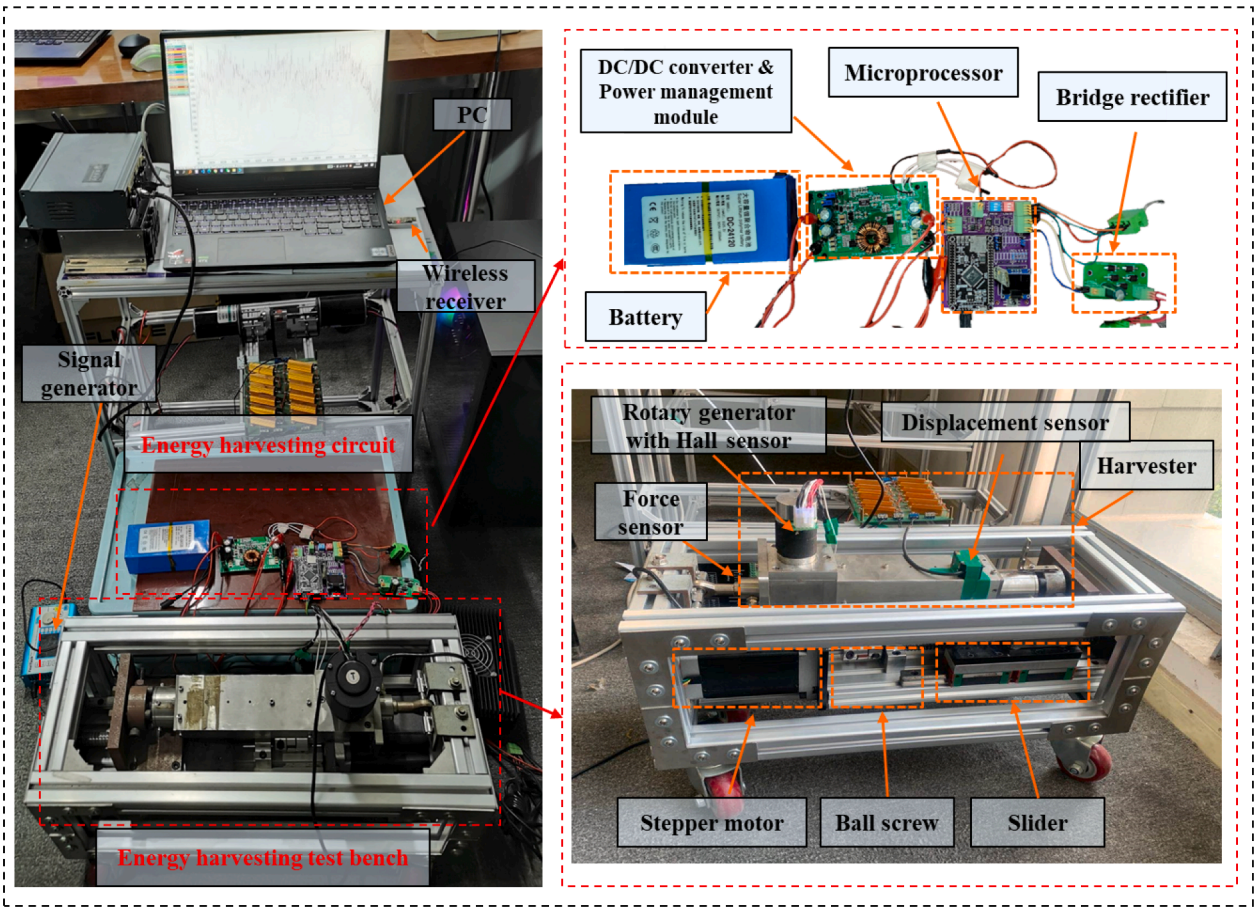

Fig. 12. Hardware implementation and experimental setup.

4.3. *Experimental validation for energy harvesting system*

Fig. 13 illustrates the experimental results of the harvester-circuit joint test under a 0.5 Hz periodic vibration excitation. The rotation velocity of the generator measured by the Hall sensor is shown in Fig. 13 **(a)**. With the speed-driven MPPT algorithm, the reference voltage V_{ref} shown in Fig. 13**(b)** is calculated based on the rotation velocity according to equation (17). Meanwhile, the measured voltage V_{dc} is well followed with the curve of V_{ref} under the closed-loop voltage control. It is noted that the speed-driven MPPT algorithm cannot work fully when the reference voltage V_{ref} is lower than the 7 V open voltage of DC/DC converter. However, the voltage of DC/DC converter is maintained around open voltage. The power is still obtained in this situation as its instantaneous curve shown in Fig. 13**(c)**. The harvester force is measured as shown in Fig. 13**(d)**, and the positive value represents the compression force, while the negative value represents the tension force. The two-period force curve corresponds to a four-period unidirectional rotation velocity and power curves, indicating that the MMR in the harvester is effective in bidirectional mechanical motion rectification and can fully harvest and utilize the bidirectional vibration energy.

The VEHS characteristics versus voltage coefficient are investigated with the integrated system model, as shown in Fig. 14. The vibration is periodic with 4 mm amplitude, and its frequency gradually increases from 0.4 Hz to 2 Hz. The average power first raises to the maximum power point (MPP), and then descends with the voltage coefficient K_v. The optimal K_v is unique, increasing from 0.45 to 0.525 with the frequency from 0.4 Hz to 1.2 Hz, and remains almost constant when the frequency is over 1.2 Hz. With the consideration of factors including the internal inductance of the generator, the dynamic impedance of the rectifier bridge, and the open voltage of DC/DC converter in the VEHS model, the optimal K_v exhibits a rightward shifting trend under a higher frequency vibration compared to the analytical value of equation (17). The RMS value of the harvester force decreases with the voltage coefficient increase because a larger K_v regulates a larger circuit impedance leading to the decrease of the harvester equivalent damping. It is noted that considering the mechanical friction in the harvester model enables the prediction of mechanical efficiency. The variation of mechanical efficiency with K_v and excitation frequency is not very regular due to its strong nonlinearity. Overall, its value increases with the decrease of K_v because the harvester damping force accounts for a larger proportion of the total force. The VEHS exhibits a better overall efficiency in a higher frequency excitation, but the efficiency is slightly reduced with the frequency increasing to 2 Hz. The optimal K_v values corresponding to the maximum efficiency points are found to be different from those of the MPP, and slightly larger than them. With the proper regulation of K_v and favorable vibration conditions, the VEHS has the potential to achieve an overall average efficiency of 42%, which is a considerable value compared to many other energy harvesting solutions.

To validate the proposed model, a series of tests were conducted with the hardware of the VEHS. The test results of average power and RMS force are shown in Fig. 14**(a) and (b)**, and the detailed results and errors between them are listed in Table 3. The VEHS model well predicts the force and shows a discrepancy ranging from 0.2% to 12.61%, which tends to become larger at conditions with a lower frequency and smaller K_v. The main reason is that some other non-ideal effects, such as the Stribeck effect, Stiction force from static frictions and backlash in mechanical transmission, are not considered in the theoretical model. The predicted power possesses a difference of −2.88% to 13.65% with the test values. In some cases where $K_v = 0.7$, the test power is larger than the predicted values. It is because the actual K_v is slightly smaller than

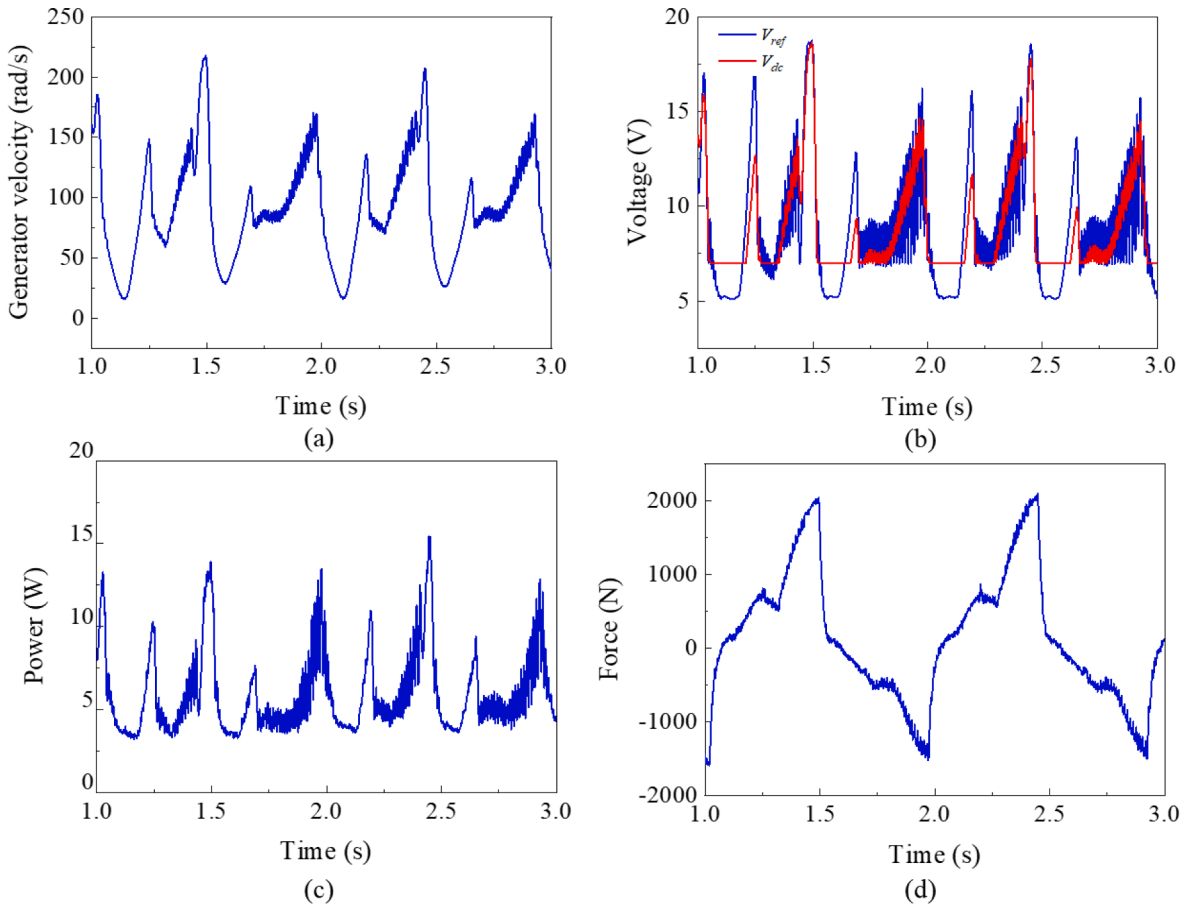

Fig. 13. Experimental results of the harvester-circuit joint test under a 0.5 Hz periodic vibration excitation: (a) rotation velocity of the generator; (b) reference voltage and measured voltage; (c) obtained power; (d) harvester force.

the ideal value, leading to the closer to MPP, and the control deviation is determined by the accuracy of the PI controller.

Overall, the effectiveness of the VEHS model is validated through the joint tests. It exhibits superior prediction accuracy and can be used as a tool for optimizing the control strategy of the harvester in onboard environments.

5. System coupling and onboard control strategy

To explore the optimization issue of speed-driven MPPT in the onboard environment, the development of the vehicle-harvester-circuit system model takes into account these practical factors: (1) the nonlinear mechanical friction in harvester modeling; (2) the open voltage of DC/DC converter, dynamic impedance of diodes, and closed-loop control of MPPT algorithm in circuit modeling; (3) nonlinearities of primary and secondary suspensions in vehicle modeling, which is introduced in **Section 5.1**. In addition, the model integration and co-simulation calculation process are presented in **Section 5.2**. **Section 5.3** reveals the optimal K_v versus vehicle speed and load with the analysis of the system model. The onboard control strategy based on the speed-driven MPPT algorithm with the dynamic tuning of K_v is proposed in **Section 5.4**.

5.1. Dynamic modeling of the freight wagon

The freight wagon, as shown in Fig. 15, is a nonlinear complex system incorporating car body, bolsters, side frames, wheelsets, and suspensions. The freight wagons with K6 bogies account for nearly half of the existing freight cars in China. The selected C80 freight wagons equipped with K6 bogies play an important role in the transportation of coal, ore, building materials, mechanical equipment, etc., on the Daqin Line (one of the most principal heavy haul freight lines in China).

To obtain an accurate solution for suspension vibration responses, the nonlinear structures of secondary and primary suspensions, as shown in Fig. 15**(e) and (f)**, have been considered. The primary suspension connecting the side frame and axlebox provides the supporting force with rubber pads. In the vertical direction, only rubber pads provide elastic deformation force for support. However, in the longitudinal and lateral directions, besides the elastic deformation force of rubber pads, the contact force between the side frame and axle box should be taken into account when they come into contact [60]. The secondary suspension includes wedges and supporting springs. The unused vibration energy is usually converted into heat by the friction of the wedges and then dissipated. The loading and unloading conditions and friction between bolster and wedges account for the nonlinearity in the secondary suspension. In addition, the harvester mounted to the secondary suspension also contributes to the force interaction. The total force of secondary suspension in the vertical direction can be presented as

$$F_{si} = K_s Z_{si} + 2F_{ws} + (-1)^k 2\mu F_{sw} + F_h \tag{19}$$

$$Z_{si} = Z_c - Z_s + (-1)^i l_t \beta_c \mp l_s \delta_c \tag{20}$$

where K_s refers to the vertical stiffness of secondary suspension springs; Z_{si} is the vertical displacement of secondary suspension where $i = 1$ or 2 represents the front or rear bogies; F_{ws} refers to the stiffness force under wedges; F_{sw} is the force between the side frame and wedges; $k = 0$ and 1 indicate the loading and unloading conditions of wedges, respectively; μ is friction coefficient; F_h is provided by the harvester; Z_c and Z_s are the

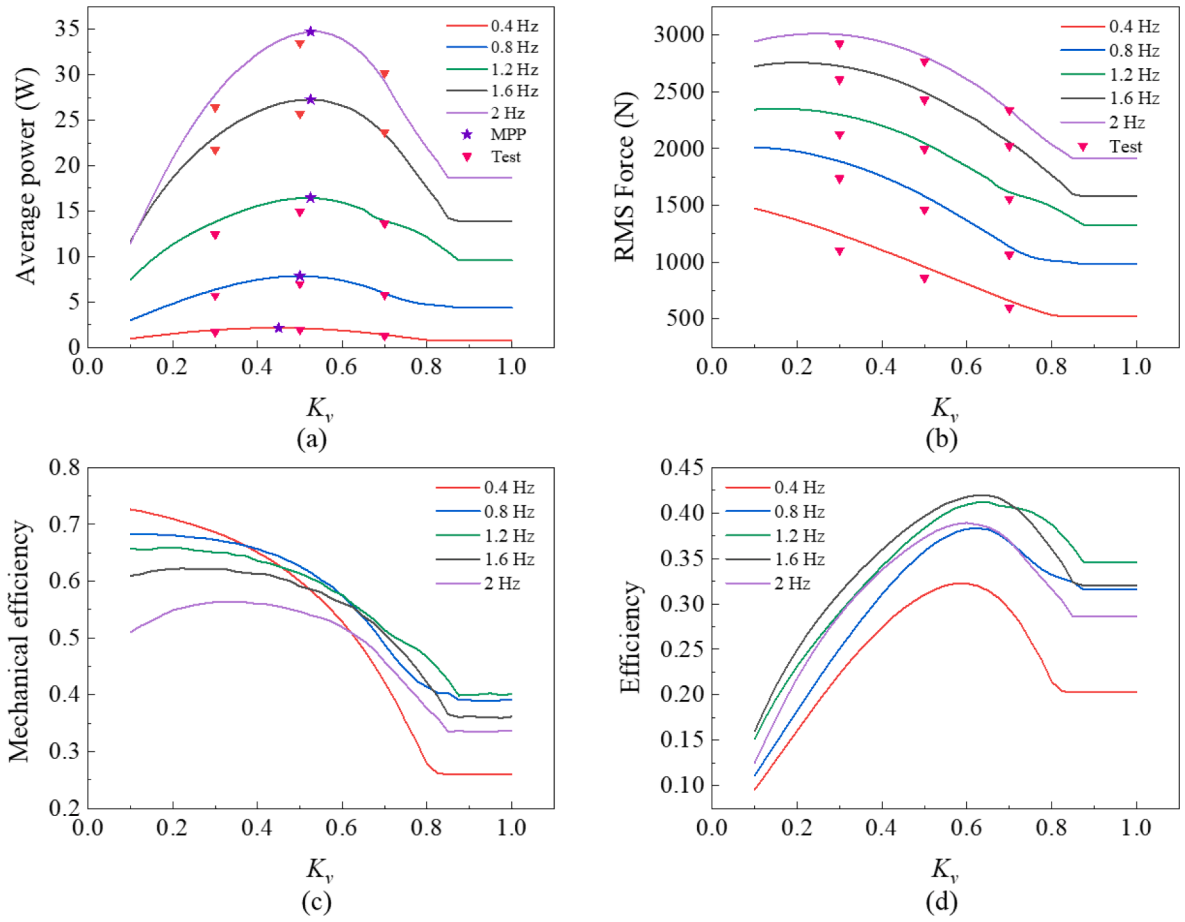

Fig. 14. Experimental validation for system characteristics: (a) average power; (b) RMS harvester force; (c) mechanical efficiency; (d) and overall efficiency versus voltage coefficient.

Table 3
Errors between test results and simulation results based on the VEHS model in average power and RMS force (positive/negative errors mean the simulation results are larger/smaller than test results).

K_v	0.3		0.5		0.7	
f /Hz	Average power	RMS force	Average power	RMS force	Average power	RMS force
0.4	13.65%	12.61%	8.68%	11.6%	7.58%	10.5%
0.8	12.31%	8.7%	12.86%	8.18%	3.65%	6.8%
1.2	11.17%	8.13%	10.08%	2.73%	2.07%	3.95%
1.6	6.41%	4.6%	5.85%	2.77%	−1%	1.83%
2	5.28%	2.77%	3.12%	1.52%	−2.88%	0.2%

bouncing of bolster and side frame; l_s and l_t represent the semi-distance between bogies in the longitudinal direction and the distance between secondary suspensions in the lateral direction; β_c and δ_c are the car body pitching and rolling motion, respectively.

To make the line situation more practical, the track irregularity of the Daqin Line was measured in site with a total detected length of 555 km at an interval of 0.25 m [61]. The power spectrum density (PSD) and generated time-domain track irregularity are shown in Fig. 15**(a) and (b)**. The wheel-rail contact is viewed as rigid, and the rail type is Chinese 60 Rail here. The dynamic model of the wagon can be governed as [62]

$$\mathbf{M}_v\ddot{Z}+\mathbf{C}_v\dot{Z}+\mathbf{K}_vZ=\mathbf{f}_r \tag{21}$$

where $\boldsymbol{M_v}$, $\boldsymbol{C_v}$, $\boldsymbol{K_v}$ correspond to the mass, damping and stiffness matrices of the wagon system, respectively; Z represents the displacement vector; and $\boldsymbol{f_r}$ refers to the force vector that indicates the wheel-rail interaction.

5.2. Integrated modeling of the vehicle-harvester-circuit system

Due to the non-negligible interaction between the freight wagon and the VEHS, the integrated modeling for the vehicle-harvest-circuit system is necessary to explore the potential harvestable power under the stochastic vibrations of freight wagon. As shown in Fig. 16, the freight wagon-track model is implemented in Simpack (a multi-body dynamic software). The VEHS consisting of the harvester module, circuit module, and control unit works in the environment of Matlab/Simulink. The co-simulation calculation is realized by the SIMAT interface in Simpack. Firstly, the wagon and track parameters should be configured in corresponding modules, followed by operation conditions including the vehicle running speed, road slope, and road curve. The time-domain track irregularity is generated based on the PSD function and input as the excitation of the dynamic model. Then, the calculated secondary vibration responses are transmitted to the VEHS model through the SIMAT interface. The harvester module accounts for calculating the force and velocity signals during mechanical transmission, and the current and voltage signals are processed in the circuit module with the closed-loop control. The harvester force signal will be returned back to the secondary suspension for the next step calculation. All data are finally processed and stored in the co-simulation interface and displayed as required.

5.3. Optimal voltage coefficient in onboard environments

Fig. 17 illustrates the instantaneous vibration velocity, harvester force, and power curves under system co-simulation when the freight wagon is fully loaded, and the voltage coefficient K_v in the speed-driven

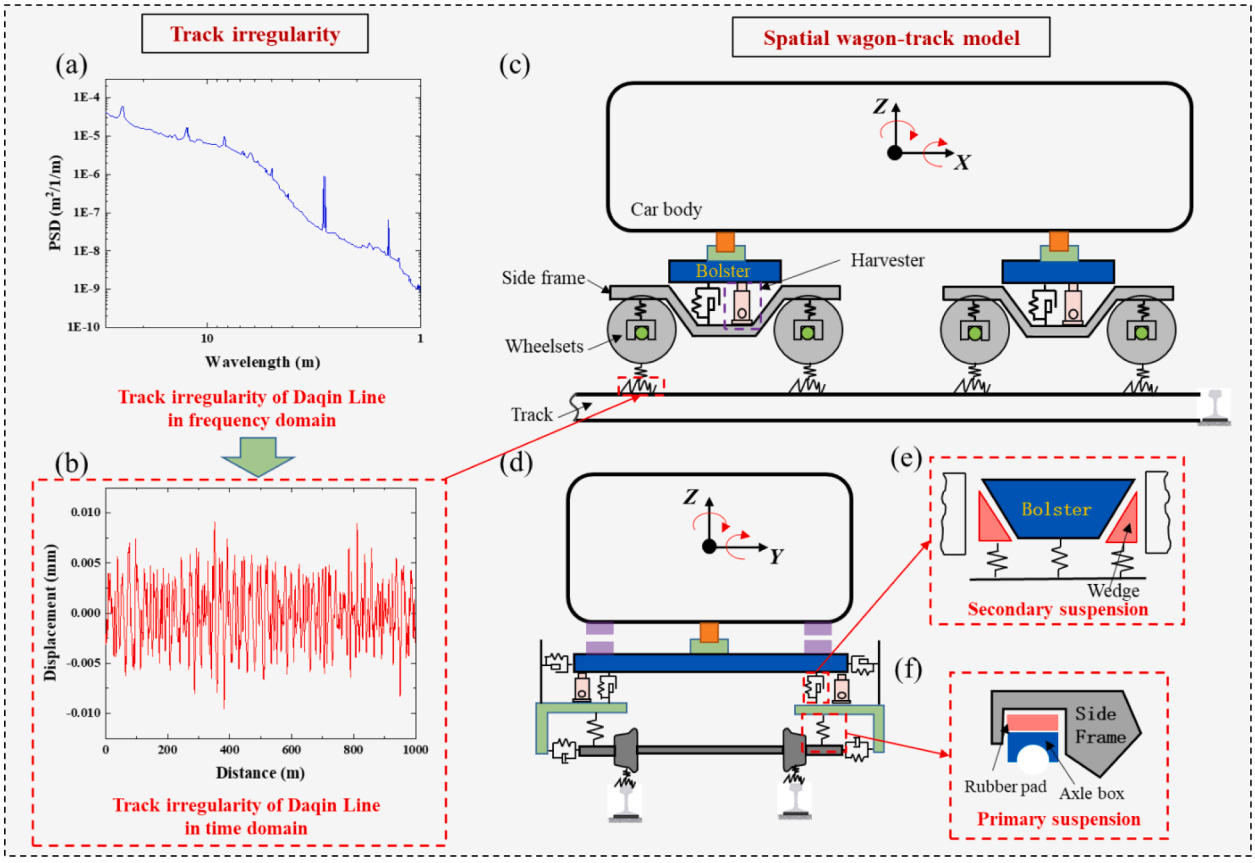

Fig. 15. Dynamic model of the wagon-track system: (a) PSD of track irregularity of Daqin Line in the frequency domain and (b) time domain; (c) side view and (d) front view of the wagon-track system; (e) nonlinear structures of (e) secondary suspension and (f) primary suspension.

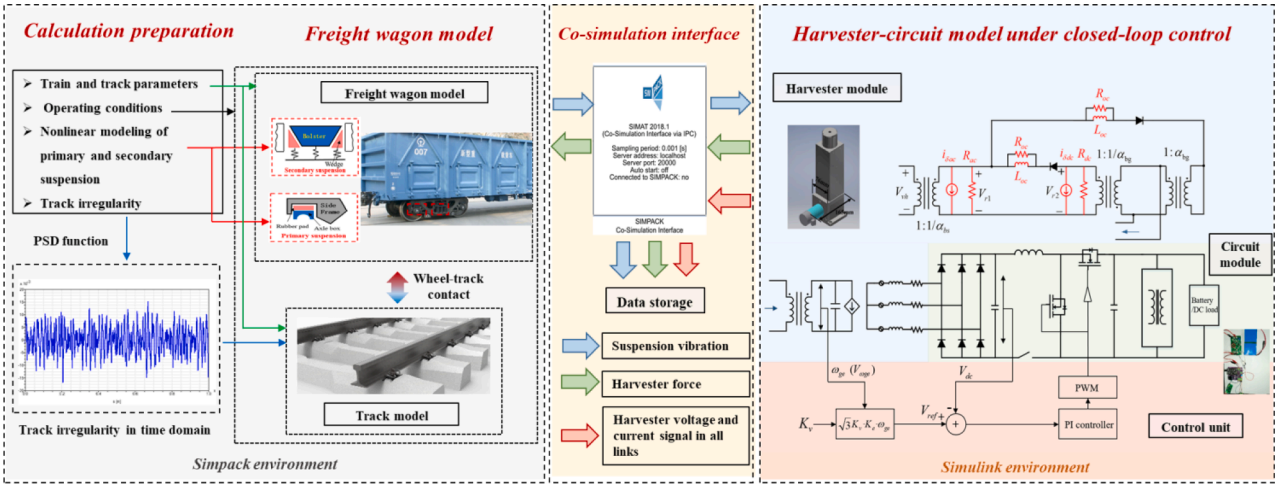

Fig. 16. Integrated modeling of the vehicle-harvester-circuit system.

MPPT algorithm is set as 0.4775 according to equation (17). The non-dimensionalized average power versus wagon load and voltage coefficient at 40, 60, and 80 km/h are summarized in Fig. 18. The nondimensionalized average power is defined as the ratio of current power to maximum power at the same speed, which can be expressed as

$$P_{non} = \frac{P_{avg}}{P_{\max\_sp}} \tag{22}$$

where P_{avg} is the average power at a particular wagon load and K_v; and P_{max_sp} represents the maximum average power at the same wagon speed.

Regardless of speed and voltage coefficient, the harvester power is positive with the wagon load until 75 t, then decreases. When the wagon speed is 40 km/h, the optimal K_v is up to 0.76 for some conditions, which is far greater than the analytically obtained optimal value of 0.4775. This is mainly because the vibration is not intense at a low wagon speed, and the generated harvester voltage hardly reaches the open voltage of DC/DC converter, a larger K_v is required to open the circuit in priority. When the wagon speed is 60 km/h, contour lines expand in all directions, and for most wagon load conditions, their nondimensionalized

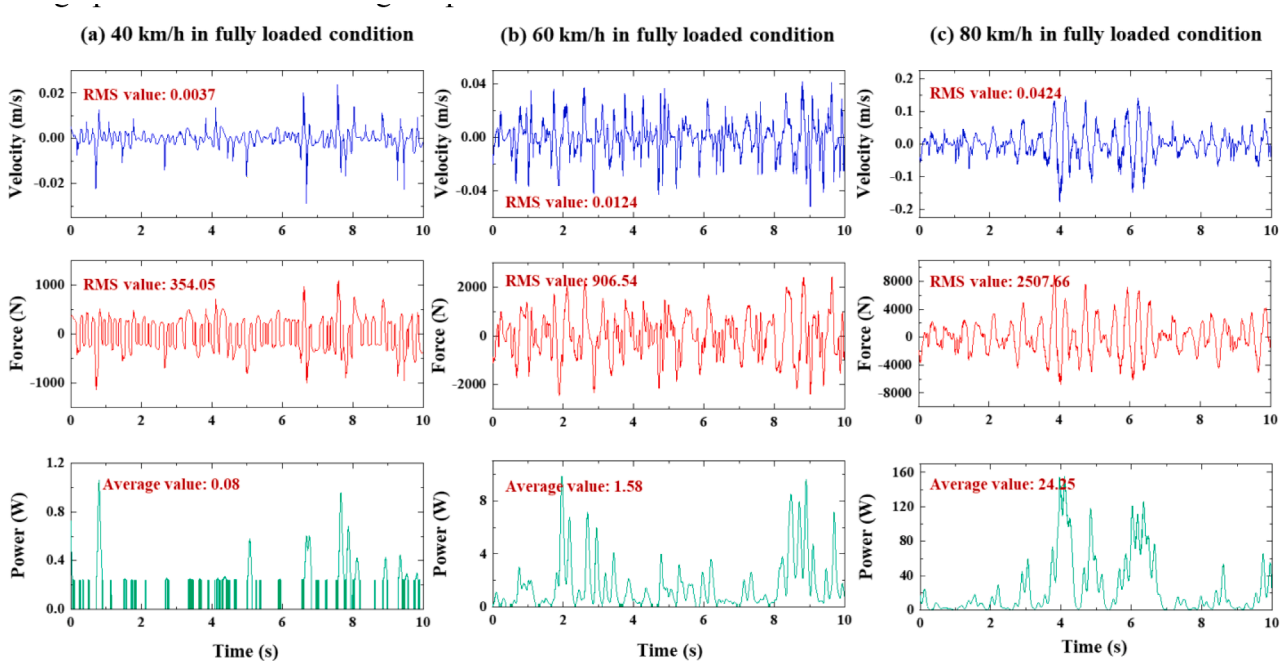

Fig. 17. Instantaneous vibration velocity, harvester force, and power curves under system co-simulation when the freight wagon is fully loaded and the voltage coefficient K_v is 0.4775 at (a) 40 km/h, (b) 60 km/h and (c) 80 km/h.

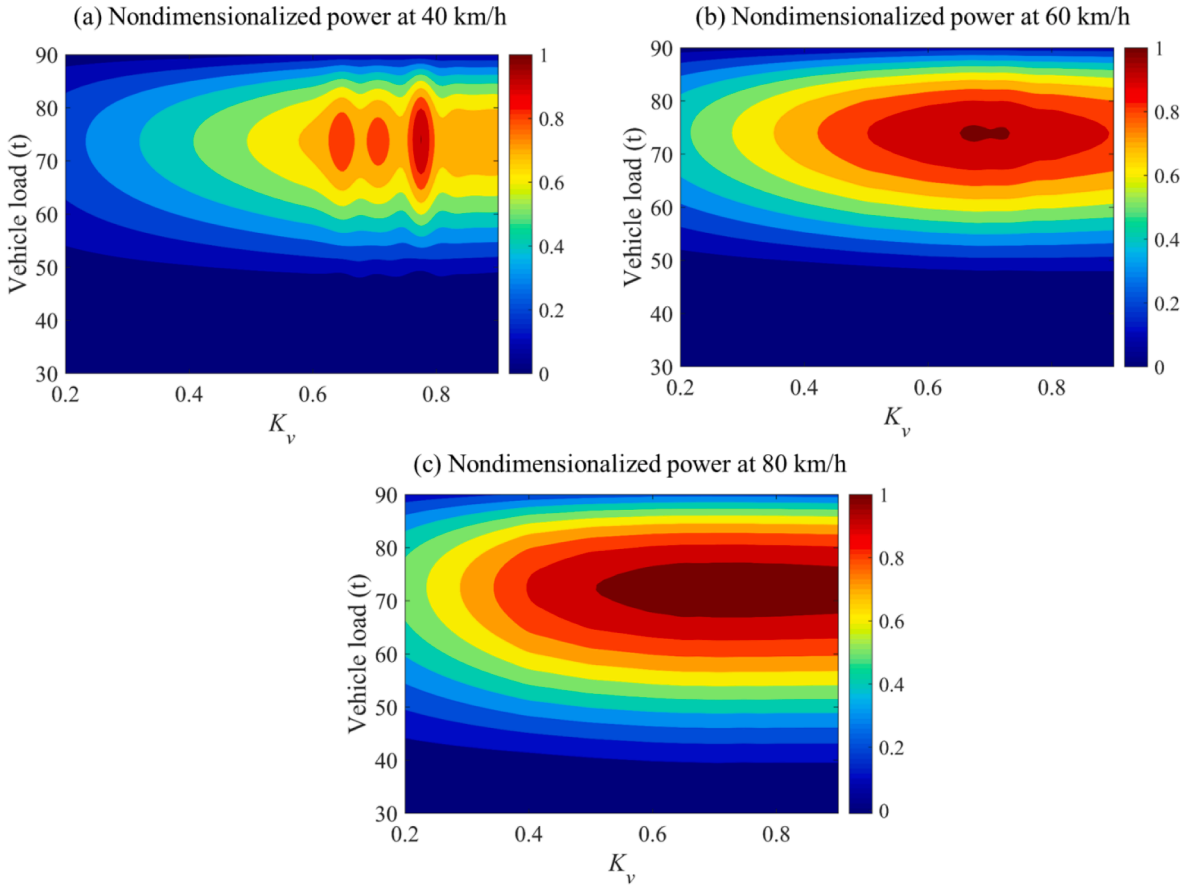

Fig. 18. Nondimensionalized average power of harvester in onboard environments versus wagon load and voltage coefficient at (a) 40 km/h; (b) 60 km/h; and (c) 80 km/h.

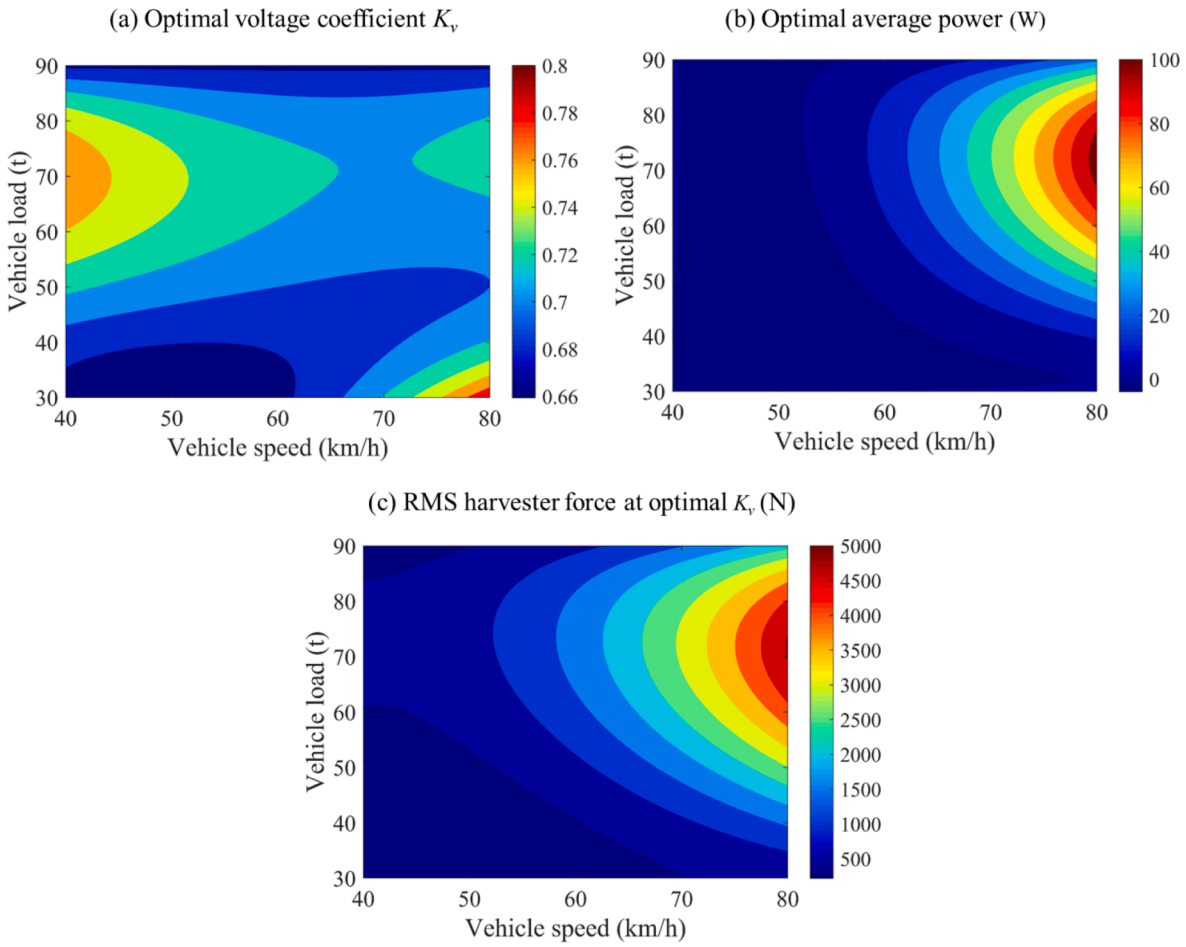

Fig. 19. Optimal system characteristics in onboard environments: (a) optimal voltage coefficient; (b) average power and (c) RMS harvester force at optimal voltage coefficient versus wagon load and speed.

average power is higher than that at 40 km/h. It indicates the power decline will not be so obvious when the K_v deviates from the optimal value. This phenomenon becomes more obvious with the wagon speed increased to 80 km/h. In addition, with the raising of wagon speed inducing a more intense vibration (the secondary vibration velocity increases significantly with the wagon speed, as shown in Fig. 17), the optimal K_v for most wagon load conditions seems to be approaching the analytical value because it is less affected by the open voltage of DC/DC converter. However, due to the existence of the force interaction between the harvester and vehicle, the optimal K_v also tends to move

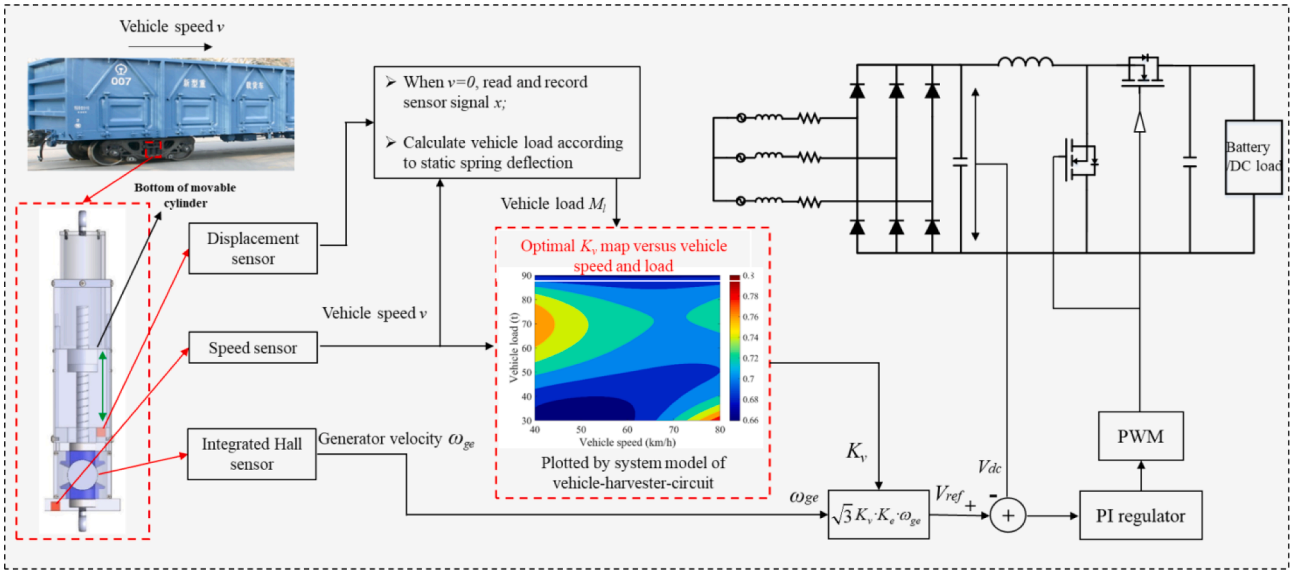

Fig. 20. Onboard control strategy for maximizing harvester power performance.

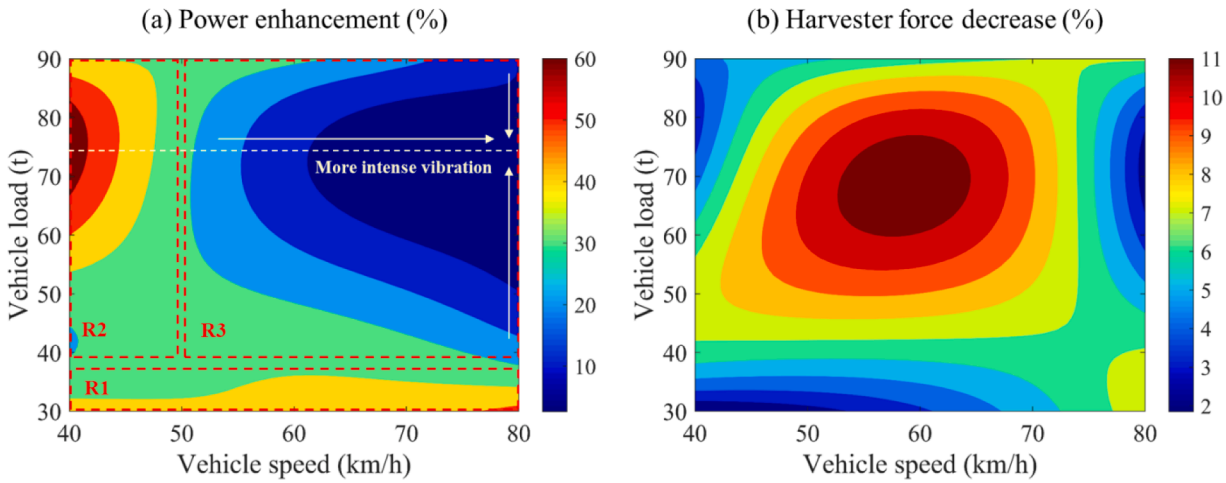

Fig. 21. Performance improvement with proposed control strategy: (a) power enhancement; (b) harvester force decrease.

rightward to reduce the weakening effect of the harvester on vehicle vibration and obtain a more conducive condition for power generation (a larger K_v will lead to a smaller harvester damping, thereby a smaller interaction force with the vehicle).

The optimal voltage coefficient K_v and the average power and RMS harvester force at optimal K_v versus wagon load and speed are illustrated in Fig. 19. The optimal K_v ranges from 0.66 to 0.8 versus wagon load and speed, which is a certain difference from the analytical value and the optimal value in Fig. 14 without the consideration of the force interaction with the vehicle. The relationship of optimal K_v with the wagon load and speed exhibits a strong nonlinearity, which is mainly caused by the following reasons: (1) K_v affects the mechanical properties of the harvester, as well as the force interaction with the vehicle, which does not always suppress the vehicle vibration, but may also slightly increase the vibration in some cases. (2) The harvester power under intense vibration is not very sensitive to K_v within a certain range with the compound influence of various factors, and a similar phenomenon appears as shown in Fig. 18**(c)**. Hence, for maximizing the onboard performance of the harvester, the optimal K_v map can be plotted in advance to guide the dynamic tuning of voltage coefficient in the speed-driven MPPT algorithm.

5.4. Onboard control strategy enhancing harvester performance

Based on the above analysis, the optimal voltage coefficient in onboard environments is related to the wagon load and speed. For maximizing harvester power performance, the onboard control strategy based on the speed-driven MPPT algorithm with the dynamic tuning of K_v is proposed, as shown in Fig. 20. An extra displacement sensor and speed sensor are embedded in the harvester. The speed sensor accounts for measuring the wagon speed. The laser displacement sensor measures and records the current distance to the bottom of the movable cylinder only when the wagon speed is 0, namely the vehicle is in a static state. The wagon load can be calculated according to

$$M_l = M_0 + n_{sp}K_s\Delta f = M_0 + n_{sp}K_s(l_0 - l_n) \tag{23}$$

where M_0 is the mass of the unloaded car body; n_{sp} is the total number of sencondary springs on a vehicle; Δf represents the spring deflection change compared to the unloaded condition and is obtained with the distance of the current measured distance l_n and the measured distance l_0 in unloaded condition.

The K_v with dynamic tuning is determined with the wagon load and speed, and participated in calculating the MPPT voltage combined with the measured generator velocity. The voltage closed-loop control part is the same as the process in the speed-driven algorithm.

Compared to the common speed-driven algorithm with the constant K_v according to equation (17), the consequent improvement with the proposed control strategy exploited is illustrated in Fig. 21. As shown in Fig. 21**(a)**, the harvester power with dynamic K_v can increase by 4% − 60% versus different wagon loads and speeds. Region 1(R1) represents light-load conditions, where considerable power enhancement is achieved because the proposed control strategy automatically increases K_v to deal with the problem that the circuit is not fully opened under a weak vibration excitation. A similar phenomenon exists in Region 2 (R2) that indicates low-speed conditions, and the enhancement around wagon load of 75 t is most significant. In Region 3 (R3), the vehicle with a heavier load runs at a higher speed. The power enhancement gets weaker under a more intense vibration with the wagon speed increasing and the wagon load approaching 75 t. Meanwhile, the harvester force decreases by 2% − 11% with dynamic K_v exploited, as shown in Fig. 21 **(b)**. This is because the optimal K_v is always larger than the theoretical analytic value, resulting in a larger circuit impedance and decreasing the harvester force. The harvester force declines obviously when the wagon load is about 70 t, and the wagon speed is around 60 km/h. The force decrease effect gets weaker with the speed and load dispersion in all directions. The proposed strategy is proven effective in enhancing the output power and decreasing the harvester force, which enables the VEHS more suitable for onboard application environments.

6. Conclusions

With the purpose of improving the performance of railway VEHSs with large-scale VEHs in onboard environments, this paper considers the complex interactions between the vehicle, harvester, and circuit by developing a comprehensive system model. Furthermore, the onboard control strategy is carefully designed with the analysis of the system model. Based on the above investigations, the following conclusions can be drawn:

(1) The equivalent circuit model of rotary electromagnetic VEH takes nonlinear mechanical friction in all mechanical transmissions and the generator into consideration. A corresponding identification approach based on the EO is proposed to determine friction parameters. The model with identified parameters is validated with high accuracy in predicting the harvester voltage and force.
(2) The EHC is modeled with the consideration of the open voltage of DC/DC converter, dynamic impedance of diodes, and closed-loop control of MPPT algorithm. The simulation results with the VEHS model indicate a discrepancy ranging from 0.2% to 12.61% in the harvester force, and a difference of −2.88% to 13.65% in the

Table A1
Parameters of the energy harvesting system for experiments.

Symbol	Value	Description	Symbol	Value	Description
L_h	370 mm	Maximum harvester height	p	8	Number of pole pairs
L_l	165 mm	Harvester Length	J_{ge}	0.181 kg. cm^2	Generator shaft inertia
L_w	76 mm	Harvester width	l	30 mm	Screw lead
L_a	83 mm	Harvester adjustable height	l_b	10 mm	Lead of screw in test bench
K_e	0.11 V/rads	Generator voltage constant	α_{bg1}, α_{bg2}	2	Bevel gear transmission ratio
K_t	0.11 Nm/A	Generator torque constant	R_i	26	Gearbox transmission ratio
R_i	6.89 Ω	Generator internal resistance	a, b,c	0.0194, −2, 0.06245	Parameters for fitting diode impedance function
L_i	5.85 mH	Generator internal inductance			

output power as compared to the test results, which confirms the model validity.

(3) The vehicle-harvester-circuit system model is integrated with the harvester-circuit module, and the spatial dynamic model of freight wagon that considers the nonlinear constructions of primary and secondary suspensions and measured track irregularity. The co-simulation results show that the optimal voltage coefficient varies from 0.66 to 0.8 depending on different vehicle loads and speeds, which has a certain difference from the analytical solution and indicates the necessity for the dynamic tuning of voltage coefficient in the speed-driven MPPT algorithm.

(4) An onboard control strategy based on the speed-driven MPPT algorithm with dynamic voltage coefficient tuning is proposed to maximize harvester power performance. With the algorithm exploited, the harvester power can increase by 4%-60%, and the harvester force decreases by 2%-11% compared to those with a constant voltage coefficient.

(5) In terms of our work in hardware and prototype manufacturing, the size and adjustable height of large-scale VEH strictly adhere to the structural constraints of wagons. The EHC integrates the speed-driven MPPT algorithm and power management module based on a synchronous 4-Switch DC/DC control chip, simultaneously dealing with impedance matching, voltage conversion, and battery charging issues, which can be a promising scheme for efficient energy extraction from large-scale VEHs. The whole VHES is validated with a series of experiments, and the next step is to carry out relevant field tests.

In summary, the carefully designed onboard control strategy can improve the performance and robustness of railway VEHSs in various conditions, making them more practical and reliable. This advancement will promote their widespread application in railway scenarios without convenient power supplies.

CRediT authorship contribution statement

Liwei Dong: Conceptualization, Data curation, Software, Writing – original draft, Writing – review & editing. **Guobiao Hu:** Project administration, Writing – review & editing. **Jie Yu:** Data curation, Validation. **Chaoyang Zhao:** Formal analysis, Software, Writing – review & editing. **Shuai Qu:** Methodology, Resources. **Yaowen Yang:** Conceptualization, Funding acquisition, Supervision, Writing – review & editing.

Declaration of Competing Interest

The authors declare that they have no known competing financial interests or personal relationships that could have appeared to influence the work reported in this paper.

Data availability

Data will be made available on request.

Acknowledgment

This work was mainly carried out by the first author during his visit to Nanyang Technological University, and sponsored by the China Scholarship Council (Grant No. 202206260157). The partial tests were supported by the National Natural Science Foundation of China (Grant No. 51728503) and the Shanghai Colabrative Innovation Research Center for Multi-network & Multi-model Rail Transit.

Appendix A

See Table A1.

References

[1] Li HC, Yu KM, Wang K, Zhang AM. Market power and its determinants in the Chinese railway industry. Transport Res Part A-Policy Pract 2019;120:261–76.
[2] Fang Z, Zhou Z, Yi M, Zhang Z, Luo X, Ahmed A. A roller-bearing-based triboelectric nanosensor for freight train synergistic maintenance in smart transportation. Nano Energy 2023;106:108089.
[3] Du Y, Tang Q, He W, Liu W, Wang Z, Wu H, et al. Harvesting ambient mechanical energy by multiple mode triboelectric nanogenerator with charge excitation for self-powered freight train monitoring. Nano Energy 2021;90:106543.
[4] Hamzat AK, Omisanya MI, Sahin AZ, Ropo Oyetunji O, Abolade ON. Application of nanofluid in solar energy harvesting devices: A comprehensive review. Energ Conver Manage 2022;266:115790.
[5] Fu XP, Bu TZ, Li CL, Liu GX, Zhang C. Overview of micro/nano-wind energy harvesters and sensors. Nanoscale 2020;12(47):23929–44.
[6] Latif U, Dowell EH, Uddin E, Yamin YM. Parametric aerodynamic and aeroelastic study of a deformable flag-based energy harvester for powering low energy devices. Energ Conver Manage 2023;280:116846.
[7] Sun R, Zhou S, Cheng L. Ultra-low frequency vibration energy harvesting: Mechanisms, enhancement techniques, and scaling laws. Energ Conver Manage 2023;276:116585.
[8] Guo C, Xu L, Su Y, Li H, Zhang M, Yang Y. Stretchable nanogenerators for scavenging mechanical energy. Nano Res 2022.
[9] Liang J, Cui R, Zhang X, Koumoto K, Wan C. Polymer/Carbon Composites with Versatile Interfacial Interactions for High Performance Carbon-Based Thermoelectrics: Principles and Applications. Adv Funct Mater 2023;33(9):2208813.
[10] Espe AE, Haugan TS, Mathisen G. Magnetic Field Energy Harvesting in Railway. IEEE Trans Power Electron 2022;37(7):8659–68.
[11] Zhao T, Xu M, Xiao X, Ma Y, Li Z, Wang ZL. Recent progress in blue energy harvesting for powering distributed sensors in ocean. Nano Energy 2021;88:106199.
[12] Zhao L-C, Zou H-X, Xie X, Guo D-H, Gao Q-H, Wu Z-Y, et al. Mechanical intelligent wave energy harvesting and self-powered marine environment monitoring. Nano Energy 2023;108:108222.
[13] Elahi H, Munir K, Eugeni M, Abrar M, Khan A, Arshad A, et al. A Review on Applications of Piezoelectric Materials in Aerospace Industry. Integr Ferroelectr 2020;211(1):25–44.
[14] Zhang RY, Hummelgard M, Ortegren J, Olsen M, Andersson H, Olin H. Interaction of the human body with triboelectric nanogenerators. Nano Energy 2019;57:279–92.
[15] Duarte F, Silva A, Barbosa M, Carvalho L. Road pavement energy harvesting: A technological, economical and cost-benefit analysis. Energy Sources Part B 2022;17(1):2109776.
[16] Tairab AM, Wang H, Hao D, Azam A, Ahmed A, Zhang Z. A hybrid multimodal energy harvester for self-powered wireless sensors in the railway. Energy Sustain Dev 2022;68:150–69.
[17] Pan HY, Jia CY, Li HB, Zhou XZ, Fang Z, Wu XP, et al. A renewable energy harvesting wind barrier based on coaxial contrarotation for self-powered applications on railways. Energy 2022;258:124842.
[18] Rahman MT, Salauddin M, Maharjan P, Rasel MS, Cho H, Park JY. Natural wind-driven ultra-compact and highly efficient hybridized nanogenerator for self-

sustained wireless environmental monitoring system. Nano Energy 2019;57:256–68.
[19] Yang F, Gao M, Cong J, Wang P. System dynamics modeling and experimental study of railway track with thermoelectric heater/generator in extreme weather conditions. J Clean Prod 2020;249:119367.
[20] Kuang Y, Chew ZJ, Ruan T, Lane T, Allen B, Nayar B, et al. Magnetic field energy harvesting from the traction return current in rail tracks. Appl Energy 2021;292:116911.
[21] Bosso N, Magelli M, Zampieri N. Application of low-power energy harvesting solutions in the railway field: a review. Veh Syst Dyn 2020;59(6):841–71.
[22] Zuo J, Dong L, Yang F, Guo Z, Wang T, Zuo L. Energy harvesting solutions for railway transportation: A comprehensive review. Renew Energy 2023;202:56–87.
[23] Hafizh M, Muthalif AGA, Renno J, Paurobally MR, Bahadur I, Ouakad H, et al. Vortex induced vibration energy harvesting using magnetically coupled broadband circular-array piezoelectric patch: Modelling, parametric study, and experiments. Energ Conver Manage 2023;276:116559.
[24] Cho JY, Jeong S, Jabbar H, Song Y, Ahn JH, Kim JH, et al. Piezoelectric energy harvesting system with magnetic pendulum movement for self-powered safety sensor of trains. Sens Actuators, A 2016;250:210–8.
[25] Sun Y, Wang P, Lu J, Xu J, Wang P, Xie S, et al. Rail corrugation inspection by a self-contained triple-repellent electromagnetic energy harvesting system. Appl Energy 2021;286:116512.
[26] Zhang LB, Dai HL, Yang YW, Wang L. Design of high-efficiency electromagnetic energy harvester based on a rolling magnet. Energ Conver Manage 2019;185:202–10.
[27] Hu G, Zhao C, Yang Y, Li X, Liang J. Triboelectric energy harvesting using an origami-inspired structure. Appl Energy 2022;306:118037.
[28] Liu Z, Zhao C, Hu G, Yang Y. A multi-degree-of-freedom triboelectric energy harvester for dual-frequency vibration energy harvesting. Mech Syst Sig Process 2023;188:109951.
[29] Zhao L-C, Zou H-X, Zhao Y-J, Wu Z-Y, Liu F-R, Wei K-X, et al. Hybrid energy harvesting for self-powered rotor condition monitoring using maximal utilization strategy in structural space and operation process. Appl Energy 2022;314:118983.
[30] Zhao L-C, Zou H-X, Wu Z-Y, Gao Q-H, Yan G, Liu F-R, et al. Dynamically synergistic regulation mechanism for rotation energy harvesting. Mech Syst Sig Process 2022;169:108637.
[31] Shan G, Zhu M. A piezo stack energy harvester with frequency up-conversion for rail track vibration. Mech Syst Sig Process 2022;178:109268.
[32] Wang Z, Wang W, Tang L, Tian R, Wang C, Zhang Q, et al. A piezoelectric energy harvester for freight train condition monitoring system with the hybrid nonlinear mechanism. Mech Syst Sig Process 2022;180:109403.
[33] Yang F, Gao M, Wang P, Zuo J, Dai J, Cong J. Efficient piezoelectric harvester for random broadband vibration of rail. Energy 2021;218:119559.
[34] Wang Y, Li S, Wang P, Gao M, Ouyang H, He Q, et al. A multifunctional electromagnetic device for vibration energy harvesting and rail corrugation sensing. Smart Mater Struct 2021;30(12):125012.
[35] Kim J. A study on the optimal design and the performance evaluation of electromagnetic energy harvesting device for the rolling stock application. J Intell Mater Syst Struct 2020;31(20):2362–77.
[36] Gong Y, Wang S, Xie Z, Shao Y, Huang W. Design, modeling and optimization of an N-shape electromagnetic energy harvester for smart bearing of high speed train. Smart Mater Struct 2021;30(7):075026.
[37] Zhang X, Zhang Z, Pan H, Salman W, Yuan Y, Liu Y. A portable high-efficiency electromagnetic energy harvesting system using supercapacitors for renewable energy applications in railroads. Energ Conver Manage 2016;118:287–94.
[38] Pan Y, Zuo L, Ahmadian M. A half-wave electromagnetic energy-harvesting tie towards safe and intelligent rail transportation. Appl Energy 2022;313:118844.
[39] Lin T, Pan Y, Chen S, Zuo L. Modeling and field testing of an electromagnetic energy harvester for rail tracks with anchorless mounting. Appl Energy 2018;213:219–26.
[40] Zhang T, Wu X, Pan Y, Luo D, Xu Y, Zhang Z, et al. Vibration energy harvesting system based on track energy-recycling technology for heavy-duty freight railroads. Appl Energy 2022;323:119673.
[41] Pan Y, Liu F, Jiang R, Tu Z, Zuo L. Modeling and onboard test of an electromagnetic energy harvester for railway cars. Appl Energy 2019;250:568–81.
[42] Li L, Wang W, Luo D, Zhang Z, Qi L, Xie L. A high-efficiency energy regeneration shock absorber based on twin slider-crank mechanisms for self-powered sensors in railway cars. Smart Mater Struct 2021;30(1):015014.
[43] Fan C, Li H, Zhang Z, Pan Y, Wu X, Ahmed A. An H-shaped coupler energy harvester for application in heavy railways. Energy 2023;270:126854.
[44] Tang L, Yang Y. Analysis of synchronized charge extraction for piezoelectric energy harvesting. Smart Mater Struct 2011;20(8):085022.
[45] Ben Ammar M, Sahnoun S, Fakhfakh A, Viehweger C, Kanoun O. Self-Powered Synchronized Switching Interface Circuit for Piezoelectric Footstep Energy Harvesting. Sensors 2023;23(4):1830.
[46] Qi Y, Xia Y. A novel switch control scheme for concise S-SSHI array interface with multiple piezoelectric energy harvesters. Microelectron J 2023;133:105703.
[47] Chen Y, Tong L, Du J, Ji H, Zhao P. An SSHC Interface Circuit for Energy Harvesting of Piezoelectric Flags. Actuators 2022;11(7):175.
[48] Zeng WT, Shi G, Hu XZ, Shi ZB, Pan JH, Sun QC, et al. A self-powered P-SSHI and boost hybrid interface circuit for Multi-PZTs and low voltage electromagnetic energy extraction. Microelectron J 2023;135:105745.
[49] Pathak M, Kumar R. Self-Propelled Pre-Biased Synchronous Charge Extraction Circuit for Triboelectric Nanogenerator. Ieee J Emerg Selected Topics Power Electron 2023;11(1):615–26.
[50] Balato M, Costanzo L, Vitelli M. MPPT in wireless sensor nodes supply systems based on electromagnetic vibration harvesters for freight wagons applications. IEEE Trans Ind Electron 2017;64(5):3576–86.
[51] Costanzo L, Lin T, Lin W, Lo Schiavo A, Vitelli M, Zuo L. Power electronic interface with an adaptive MPPT technique for train suspension energy harvesters. IEEE Trans Ind Electron 2021;68(9):8219–30.
[52] Costanzo L, Schiavo AL, Vitelli M, Zuo L. Optimization of AC/DC Converters for Regenerative Train Suspensions. IEEE Trans Ind Appl 2022;58(2):2389–99.
[53] Jung H, Sharma Y, Zuo L. Digitally Controlled Power Management Circuit With Dual-Functioned Single-Stage Power Converter for Vibration Energy Harvesting. Ieee J Emerg Selected Topics Power Electron 2022;10(4):3873–82.
[54] Tianchen Y, Jian Y, Ruigang S, Xiaowei L. Vibration energy harvesting system for railroad safety based on running vehicles. Smart Mater Struct 2014;23(12):125046.
[55] Gao M, Yang F, Wang P. Symplectic analysis of stationary random vibration of vehicle–track coupled system with rail-borne electromagnetic generator. Adv Mech Eng 2018;10(10).
[56] Pan Y, Lin T, Qian F, Liu C, Yu J, Zuo J, et al. Modeling and field-test of a compact electromagnetic energy harvester for railroad transportation. Appl Energy 2019;247:309–21.
[57] Li Z, Zuo L, Kuang J, Luhrs G. Energy-harvesting shock absorber with a mechanical motion rectifier. Smart Mater Struct 2013;22(2):025008.
[58] Chen C, Li X, Zuo L, Ngo KDT. Circuit Modeling of the Mechanical-Motion Rectifier for Electrical Simulation of Ocean Wave Power Takeoff. IEEE Transactions on Industrial Electronics 2020;68(4):3262–72.
[59] Faramarzi A, Heidarinejad M, Stephens B, Mirjalili S. Equilibrium optimizer: A novel optimization algorithm. Knowl-Based Syst 2020;191:105190.
[60] Zhang D, Zhai W, Wang K. Dynamic interaction between heavy-haul train and track structure due to increasing axle load. Aust J Struct Eng 2017;18(3):190–203.
[61] Hao X, Yang J, Yang F, Li H, Qin H, Hou Y. Analysis and expression of track irregularity spectrum of heavy-haul railway. J China Railway Soc 2022.
[62] Zhai W, Wang K, Cai C. Fundamentals of vehicle–track coupled dynamics. Veh Syst Dyn 2009;47(11):1349–76.